Monthly Notices
of the
ROYAL ASTRONOMICAL SOCIETY

MNRAS **438,** 573–589 (2014)
Advance Access publication 2013 December 21

doi:10.1093/mnras/stt2227

Production of EMRIs in supermassive black hole binaries

J. Nate Bode[1,2]★ and Christopher Wegg[1,3]★

[1]*Theoretical Astrophysics, California Institute of Technology, M/C 350-17, Pasadena, CA 91125, USA*
[2]*Boston Consulting Group, 300 N. LaSalle Ave, Chicago, IL, 60654, USA*
[3]*Max-Planck-Institut für Extraterrestrische Physik, Giessenbachstrasse, D-85748 Garching, Germany*

Accepted 2013 November 14. Received 2013 September 17; in original form 2013 July 23

ABSTRACT

We consider the formation of extreme mass-ratio inspirals (EMRIs) sourced from a stellar cusp centred on a primary supermassive black hole (SMBH) and perturbed by an inspiraling less massive secondary SMBH. The problem is approached numerically, assuming the stars are non-interacting over these short time-scales and performing an ensemble of restricted three-body integrations. From these simulations, we see that not only can EMRIs be produced during this process, but the dynamics are also quite rich. In particular, most of the EMRIs are produced through a process akin to the Kozai–Lidov mechanism, but with strong effects due to the non-Keplerian stellar potential, general relativity and non-secular oscillations in the angular momentum on the orbital time-scale of the binary SMBH system.

Key words: black hole physics – gravitational waves – stars: kinematics and dynamics.

1 INTRODUCTION

One of the most interesting sources for low-frequency gravitational wave (GW) detectors such as the final incarnation of the *Laser Interferometer Space Antenna* (*LISA*), or its newer scion European *LISA* (*eLISA*), is the capture of stellar mass compact objects (COs) by a supermassive black hole (SMBH). COs are the final state of stellar evolution and include stellar mass black holes, neutron stars and white dwarfs. Due to the significant mass difference between the SMBH and the inspiraling CO, these sources are referred to as extreme mass-ratio inspirals (EMRIs).

Detection of EMRIs by GW detectors provides: (1) an accurate measurement of the spin and mass of the SMBH (Barack & Cutler 2004) along with a moderate determination of its location, (2) a test that the spin and mass are the only parameters characterizing the black hole's space–time (termed 'bothrodesy'; Ryan 1997; Hughes 2009), (3) information about the presence of a secondary SMBH orbiting the primary SMBH (Yunes, Miller & Thornburg 2011a), (4) information about the presence of a gaseous disc in the system (Narayan 2000; Yunes et al. 2011b) and (5) a possible electromagnetic counterpart to the *LISA* signal (Menou, Haiman & Kocsis 2008; Sesana et al. 2008a), if the source was a white dwarf. Such an electromagnetic counterpart would localize the host, thus allowing for follow-up observation.

The production of EMRIs amounts to either forming COs on, or driving them on to, orbits whose GW inspiral time is shorter than the time-scale for other orbital perturbations. The standard method of EMRI production (Hils & Bender 1995) is that COs are transported to the EMRI loss cone via gravitational scattering with other stellar mass objects. This is an improbable event because, as the CO's orbit becomes more eccentric and the rate of orbital energy loss to GW emission increases, ever smaller kicks to its angular momentum may remove it from this orbit or plunge it directly into the central SMBH. Despite the apparent unlikeliness of this process, many such EMRIs are expected to form, and be observable by low-frequency GW missions (see Amaro-Seoane et al. 2007, for a review of the subject).

Other possible EMRI formation mechanisms include the in situ formation of COs via a massive self-gravitating accretion disc (Levin 2003) like that which is believed to have existed in the Milky Way (Levin & Beloborodov 2003). Alternatively, the CO can be deposited close to the SMBH by a stellar binary which interacts strongly with the SMBH and ejects the CO's partner, while leaving the CO on a low-eccentricity orbit with small semimajor axis (Miller et al. 2005).

We consider a different scattering method; one where a secondary SMBH is present and entering the final stage of its inspiral (Begelman, Blandford & Rees 1980; Milosavljević & Merritt 2003) due to dynamical friction. In this scenario, the scattering phase is short lived, but the rate of stars scattered to highly eccentric orbits is significantly increased. Moreover, the secondary SMBH induces Lidov–Kozai oscillations in the orbital elements of many stars, considered first in the context of tidal disruptions by Ivanov, Polnarev & Saha (2005). Because some of these stars are COs, on passages close to the primary SMBH, they are not tidally disrupted, but instead radiate a fraction of their orbital energy in GWs, leaving for the possibility of ultimately becoming an EMRI.

We investigate this possibility by performing an ensemble of three body integrations. The equations of motion of a star randomly

★ E-mail: natebode@gmail.com (JNB); wegg@mpe.mpg.de (CW)

chosen from a stellar cusp centred on a primary SMBH are integrated in the presence of a secondary SMBH inspiraling on a pre-calculated path determined by dynamical friction (Section 3.6). We consider a $10^6\,M_\odot$ primary SMBH and various masses of the secondary SMBH and stars. The stars are then followed to determine if they eventually become EMRIs. For clarity, we add that throughout the epochs of SMBH binary evolution we consider GW radiation has no practical effect on the SMBH orbit.

We present the results as follows. In Section 2, we present a brief introduction to EMRI formation under the standard channel, while we describe the assumptions and physical setup in Section 3. The simulation is described in Section 4 and the resulting rates are provided in Section 5. To understand the dynamics which result in the majority of our EMRIs, we elucidate the standard Kozai–Lidov mechanism, as well as extensions, in Section 6. Our rates and the relevance of the assumptions they are based on are discussed in Section 7. In Section 8, we present our conclusions.

2 BACKGROUND

2.1 Parameter space

Many of the key aspects of the standard method of EMRI formation are illustrated in Fig. 1 where we plot $a(1-e)$ as a function of a, where a and e are the stars' semimajor axis and eccentricity, respectively. A star lying in this region of parameter space will inspiral due to GW radiation along curves like the solid red lines, and would take approximately the period of time labelled along the blue dashed lines to complete the inspiral, assuming no other interactions. Both are calculated using the approximate expressions in Peters (1964). A star lying below the solid grey line would likely turn into an EMRI, while one above would likely undergo some stellar scattering event which would increase its angular momentum (moving it upwards in the figure) and ultimately put it on a new trajectory with a much longer inspiral time. For reference and illustrative purposes, we also plot the initial conditions of the 10^6 stars we simulate. These stars

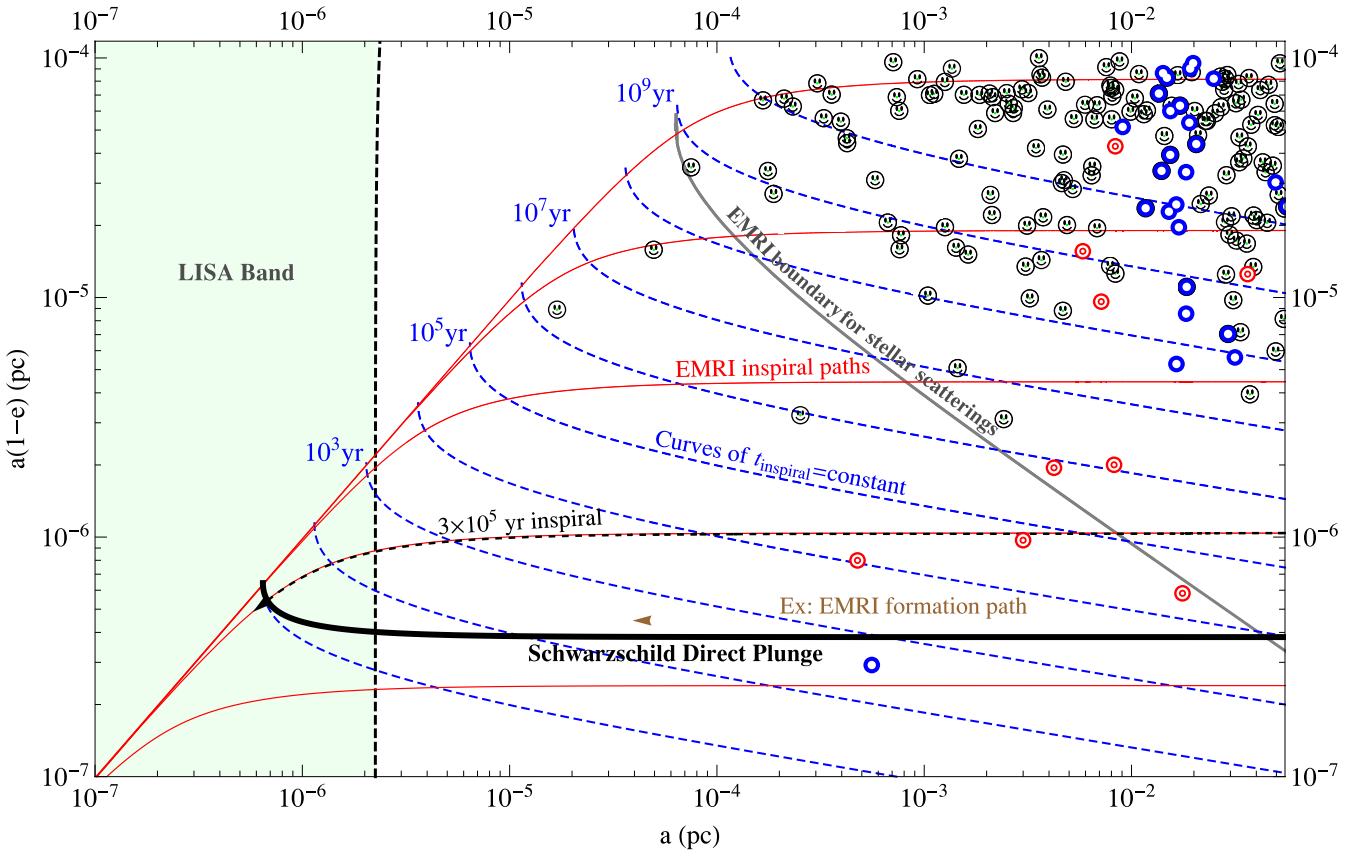

Figure 1. The standard EMRI parameter space with new addition. We plot $a(1-e)$ as a function of a with a and e defined by equations (1) and (2), respectively. A CO (stellar-mass black hole, neutron star, white dwarf) inspirals due to GW radiation along paths shown in solid red and approximated using the far-field equations of Peters (1964). The time-scale for inspiral is approximately given by the times on the dashed blue curves, which are also calculated from Peters (1964). However, if no secondary SMBH is present and if the initial $\{a, a(1-e)\}$ pair lies above the solid grey line, the star is unlikely to complete its inspiral before two-body stellar scatterings move the orbit to larger $a(1-e)$. The minimum angular momentum a star can have while on a parabolic orbit without plunging into the primary SMBH, $L_{\rm plunge}$ (also referred to as the unstable circular orbit or separatrix), is plotted in thick solid black. In our simulation with mass ratio $q = 0.3$ and stellar masses $m_\star = 10\,M_\odot$, the red targets are the initial conditions of a star which turned into an EMRI, the thick blue circles are the initial conditions for stars which turn into plunges, and the smiley faces are the initial conditions for stars who end the simulation uneventfully. We use the same initial conditions for all of our simulations, though which stars become EMRIs, plunges or neither obviously differs. As an example of a star formed from the presence of a secondary SMBH we show in solid brown the path of one of the EMRIs produced in our simulations. The star is also marked as a red-outlined gold star in Figs 4, 6 and 7 and used to demonstrate the importance of precession due to the SP and GR in Fig. 3. This star has a path similar to many seen in our simulations, elucidating the new channel of EMRI production.

are also appropriate for the standard EMRI formation, since they are drawn from a stellar distribution (equation 4) in the absence of the secondary. For these highly eccentric orbits, in the standard EMRI picture, weak stellar scatterings extract or add angular momentum from a star while keeping its energy approximately constant. This moves the star up or down in the figure. When the star scatters below the grey line, gravitational radiation can extract energy from the orbit faster than it is likely to be perturbed by star–star scatterings, thus leaving the star to inspiral along the red lines.

In the case presented in this paper, the picture is similar, but more intricate and rich. Kozai oscillations, along with significant apsidal precession due to the stellar potential (SP) and general relativity (GR), drive the stars on an orbital evolution which also conserves the orbital energy while causing the angular momentum to rise and fall before a close passage with the primary SMBH occurs. If the star passes close enough to the primary SMBH that a significant fraction of the star's orbital energy can be radiated in GWs, it can quickly circularize and form an EMRI. To elucidate these points the path of an EMRI formed in one of our simulations is shown in thin solid brown. The same star is also marked by a red-outlined gold star in Figs 4, 6 and 7 and used to demonstrate the relative importance of the SP and GR in Fig. 3. Like many of the EMRIs formed in our simulations, this star begins with a low-eccentricity orbit and with a semimajor axis about a factor of 10 smaller than the stalling radius of the secondary SMBH. It is only through an intricate interplay between the Kozai effect, precession due to the SP (SP precession) and GR effects that the star is driven to high eccentricity, has strong interactions with the primary SMBH and ultimately forms an EMRI.

2.2 Nomenclature and notation

In general, we write quantities relevant to the primary SMBH without subscripts, those relevant to the secondary SMBH with a subscripted large black 'dot', and those relevant to the stars with a subscripted star symbol. For example, the mass of the primary SMBH hole is written M, while those of the stars and secondary are written $m_\star$ and $M_\bullet$, respectively. Similarly the semimajor axes of any given star and the secondary are written $a_\star$ and $a_\bullet$. Note, however, that the subscript is foregone in figure labels. The mass ratio of the two SMBHs is denoted $q \equiv M_\bullet/M \leq 1$. We summarize the notation used in this work in Table 1.

Because of the non-Keplerian potential (due to the SP, the secondary SMBH and GR) there can be ambiguity when referring to the Keplerian orbital elements. We use unambiguous analogous quantities to the Keplerian orbital elements to describe the orbits of our stars. A star's semimajor axis, $a_\star$, is defined to be a function of the star's energy, E,

$$a_\star \equiv \frac{GM}{2E}\,, \tag{1}$$

while the eccentricity is defined using the reduced angular momentum, L, and $a_\star$:

$$e \equiv \sqrt{1 - \frac{L^2}{GMa}}\,. \tag{2}$$

In these expressions, E and L are calculated in the primary SMBH's frame rather than the centre of mass frame. These are the quantities shown in the figures unless stated otherwise.

Since in static non-Keplerian potentials L and E are conserved along orbits, then, provided the secondary's orbital period is long compared to a given star's, on the star's orbital time-scale both a and e defined as above are well-defined quantities and have minimal variations. Moreover, they are consistent with the standard definitions for the Keplerian orbital elements in the limit of Keplerian orbits.

The orbits which are interesting to us are those which approach the inner several Schwarzschild radii but have semimajor axes relatively close to the secondary SMBH; i.e. these orbits are highly eccentric. In this case,

$$L^2 \approx 2GMa(1-e) \propto a(1-e)\,. \tag{3}$$

The right-hand side of this equation is just the equation for the Keplerian periapsis distance in the limit of a Keplerian orbit. Because of this correspondence to both the angular momentum in these high-eccentricity orbits and its correspondence to the periapsis distance in the Keplerian limit, we frequently plot $a(1-e)$ and refer to it as the periapsis distance.

Stars whose angular momentum is less than $L_{\rm plunge} \equiv 4GM/c$ on a close approach to an SMBH find themselves on a one-way trip to the black hole, 'plunging' across the event horizon. This corresponds to a periapsis distance in Schwarzschild radial coordinate of $4GM/c^2$ (see equation 11), however in $a(1-e)$, $L_{\rm plunge}$ corresponds to $8GM/c^2$.

3 PHYSICAL SETUP

3.1 The outline

Throughout this paper, the system we are considering is made up of three objects: (1) a primary SMBH surrounded by (2) a stellar cusp of mass equal to twice the primary's mass and (3) orbited by a secondary SMBH. We simulate this system by assuming that the stars in the cusp are non-interacting, allowing us to reduce the problem to a series of three-body problems which are made up of the primary SMBH, the secondary SMBH and a star selected randomly from a stellar distribution.

In particular, we use a modified version of the simulation code used to study tidal disruptions in (Wegg & Bode 2011, hereafter WB11, see Section 4 for differences). There we were interested in the possibility of observing multiple tidal disruptions from the same galaxy due to the presence of a secondary SMBH. The similarities to the problem considered here make this code particularly appropriate.

We initially distribute stars isotropically according to an η-model (Tremaine et al. 1994) for a single-mass stellar distribution around the primary SMBH (Section 3.3). However, we truncate the SP just inside the stalling radius of the secondary (Section 3.4). The secondary is then spiralled inwards on a slightly eccentric orbit approximating the orbit of an SMBH evolving by dynamical friction and stellar ejection (Section 3.6), but smoothly stopping the inward motion at the stalling radius (Sesana, Haardt & Madau 2008b). The primary difference between WB11 and here is that now we must take into account relativistic effects (Section 3.7) to properly model the stellar dynamics.

3.2 The initial conditions

We run four simulations, where we have varied two parameters: the SMBH mass ratio which is chosen to be either $q = 0.1$ or 0.3 and the stellar mass which is chosen to be either $1\,{\rm M}_\odot$ or $10\,{\rm M}_\odot$. The simulations are not independent, since we use the same initial velocities and positions for the 10^6 stars simulated in all of the simulations. This is significantly quicker computationally because,

Table 1. Notation: equations and descriptions of parameters and variables listed in alphabetical order.

Parameter	Description	Equation number
$a_\star$	Semimajor axis of a star	Equation (1)
$a_\bullet$	Semimajor axis of secondary SMBH	n/a
c	Speed of light	n/a
e	Eccentricity	Equation (2)
E	Specific orbital energy	Section 2.2
G	Gravitational constant	n/a
i	Inclination	n/a
L	Total specific angular momentum	Equation (3)
L_z	z component of specific angular momentum, SMBH binary lies in x–y plane	n/a
$L_{\rm plunge}$	Angular momentum below which stars plunge into SMBH, equal to $4GM/c$	n/a
M	Mass of primary SMBH	n/a
$M_\star(< r)$	Stellar mass interior to r	Equation (5)
$M_\bullet$	Mass of secondary SMBH	n/a
$m_\star$	Mass of compact remnant	n/a
$P_\star$	Period of star's orbit	n/a
$P_\bullet$	Period of secondary SMBH's orbit	n/a
q	Mass ratio of secondary to primary SMBH	n/a
r	Radial position from primary SMBH	Section 3.3
$r_{\rm c}$	Characteristic size of cusp	Section 3.3
$R_{\rm Stall}$	Stalling radius of secondary	Section 3.6
$T_{\rm Kozai}$	Kozai time-scale	Equation (23)
$t_{\rm Kozai}$	Instantaneous Kozai period	Equation (35)
$t_{\phi,{\rm GR}}$	Time for orbit to precess by π radians due to GR	Section 6.4
$t_{\phi,\,{\rm SP}}$	Time for orbit to precess by π radians due to SP	Section 6.4
$U(r)$	Total gravitational potential	Equation (9)
v	Velocity	n/a
$\Delta L_{\rm b}$	Oscillations in L_z on the time-scale of the secondary SMBH's orbit	Section 6.6
$\Delta L_\star$	Oscillations in L_z on the time-scale of the stellar orbit	Section 6.7
η	Parameter for cusp steepness	Section 3.3
$\rho_\star$	Density of stars	Equation (4)
$\rho_\star(< v)$	Density of stars with velocity less than v	n/a

for simulations with the same q, we only reintegrate orbits that pass within $100\,GM/c^2$, the only region the stars' mass impacts its trajectory (which is only important when considering GR effects: see Section 4.2). Additionally, it also provides a direct comparison between the stars from each simulation which form EMRIs.

We choose a primary SMBH mass of $M = 10^6$ M$_\odot$ for all of our simulations since this will result in EMRIs with frequencies best suited for detection by low-frequency space-based GW detectors such as *LISA* (Amaro-Seoane et al. 2007) or *eLISA* (Amaro-Seoane et al. 2012). The 10^6 stars are given initial positions and velocities appropriate for a relaxed isotropic cusp centred on the primary SMBH (Section 3.3).

3.3 The stellar distribution

We integrate stars drawn from a cusp centred on the primary SMBH. The initial orbits of the stars are drawn from the self-consistent isotropic potential-density pair known as the η-model, meaning that the initial stellar distribution is drawn from (Tremaine et al. 1994, with $\mu = 0.5$)

$$\rho_\star(r) = \frac{\eta}{2\pi r_{\rm c}^3}\frac{M}{\left(\frac{r}{r_{\rm c}}\right)^{3-\eta}\left(1+\frac{r}{r_{\rm c}}\right)^{1+\eta}}\,, \tag{4}$$

where $r_{\rm c}$ is the characteristic size of the cusp and η is a dimensionless parameter controlling the central steepness of the cusp. The stellar mass interior to radius r is therefore given by

$$M_\star(< r) \equiv M_{\star,\eta}(< r) = \frac{2\,Mr^\eta}{(r_{\rm c}+r)^\eta}\,. \tag{5}$$

Throughout this work, we use $\eta = 1.25$ since this is the relaxed form of the distribution close to the SMBH (Bahcall & Wolf 1976). Our choice is motivated by Freitag, Amaro-Seoane & Kalogera (2006) who simulate multimass models of stellar cusps finding mass segregation close to the black hole. In that work, the most massive species are steeper than $\eta = 1.25$ and less massive species less steep. However the overall density is close to $\eta = 1.25$.

We discuss the consequences of our assumption of a universal $\eta = 1.25$ in Section 7 and of mass segregation when calculating the rates in Section 5.2.

3.4 Stellar distribution: static, fixed and truncated

To reduce computational complexity, we fix the SP to the primary SMBH and do not evolve it in time. Though this is clearly inconsistent, since the secondary SMBH scatters stars on to new orbits and therefore modifies the SP, most of our EMRIs are sourced from a tenth of the stalling radius where these modifications are not significant. We discuss this in more detail in Section 7.2 and demonstrate the magnitude of the error in Fig. 8.

However, without modification there would be a different inconsistency of much greater import. It is important that the pre-calculated SMBH path is consistent with the integrated test particle equations of motion. If an inconsistency is present then a particle

orbiting close to the primary has an incorrect acceleration towards the secondary. This would represent an unphysical dipole-like perturbation, which would typically dwarf the smaller tidal quadrupole perturbation due to the secondary. An inconsistency of this type would arise if equation (5) was used as the SP fixed to the primary, while the secondary orbit was calculated using equation (7), where only the stellar mass interior to the secondary's orbit appears.

Instead, the SP is truncated marginally inside the stalling radius. This has the result that the potential and stellar density are no longer self-consistent outside the stalling radius. However, stars outside the stalling radius that closely approach the SMBHs have undergone strong chaotic interactions with the binary. Therefore, having a fully consistent SP is less important in this region than for stars close to the primary which undergo secular interactions. For these inner stars we have the correct potential, and therefore the correct secular evolution.

3.5 Parameters of the stellar cusp

Throughout we use a fiducial cusp radius $r_c = 1.7$ pc. This is motivated by the fits from Merritt, Schnittman & Komossa (2009) to the inner regions of Virgo Cluster galaxies (Côté et al. 2004). For power-law galaxies these give[1]

$$r_{\rm inf} = 22\,(M/10^8\,{\rm M}_\odot)^{0.55}\,{\rm pc}\,, \tag{6}$$

where $r_{\rm inf}$ is defined such that the stellar mass interior to $r_{\rm inf}$ is $2\,M$, and M is the mass of the SMBH. Matching this to the η-model such that the central densities are equal gives $r_c = r_{\rm inf}$. Extrapolating to Sgr A* which has a mass of $\approx 4 \times 10^6$ M$_\odot$ (Ghez et al. 2008) gives $r_{\rm inf} = 3.8$ pc which agrees well with the observations of $r_{\rm inf} \approx 4$ pc (Alexander 2005). Using $M = 10^6$ M$_\odot$ gives our fiducial $r_{\rm inf} = r_c = 1.7$ pc.

We note that using a total stellar mass which is twice that of the primary SMBH has the convenient property that when matching the central density to a power law, r_c happens to be the radius at which the mass enclosed by the power law is $2\,M$ (the total stellar mass). This allows easy comparison with measurements.

3.6 The inspiral of the secondary

Initially the stars are on orbits consistent with the primary SMBH and the SP. Subsequently their orbits are perturbed by interaction with the secondary SMBH as it inspirals to its stalling radius. In a fully self-consistent simulation, the orbit of the secondary would evolve due to this exchange of energy with the stars. Instead, for efficiency and simplicity we calculate the orbit of the secondary SMBH assuming an inspiral dominated by dynamical friction with an appropriate Coulomb logarithm such that it stalls at the stalling radius.

Specifically, the secondary SMBH is, at time $t = 0$, given an eccentricity of approximately 0.1 and an initial separation equal to the cusp radius, r_c. It is then migrated inwards on a path governed by

$$\frac{{\rm d}\boldsymbol{v}}{{\rm d}t} = -\frac{G\,[M(1+q) + M_\star(<r)]}{r^3}\boldsymbol{r} - \frac{\boldsymbol{v}}{t_{\rm df}}, \tag{7}$$

where $M_\star(<r)$ is the stellar mass interior to r and

$$t_{\rm df} = \frac{v^3}{2\pi G^2 \log\Lambda\, M q\, \rho_\star(<v)} \tag{8}$$

characterizes the dynamical friction (Binney & Tremaine 2008). Here $\rho_\star(<v)$ is the density of stars at r with velocity less than v. We have used a Coulomb logarithm that begins at $\log\Lambda \approx 4$, but which smoothly decreases to zero at the stalling radius calculated by Sesana et al. (2008a). The functional form of the decrease was chosen to approximate the rate of shrinkage caused by the energy exchange with the stars during our simulations. This approximation was checked in WB11.

All the simulations in this work are all of length $45\sqrt{r_c^3/GM} \approx 1.5$ Myr. We assume that the secondary SMBH remains near its stalling radius for this duration. Our choice of simulation termination is arbitrary and was chosen to limit computation time: the rate of EMRIs and direct plunges has significantly dropped but not yet fallen to zero at the end of the simulations. We repeated one of the simulations for four times the duration to assuage fears that only a small fraction of the total number of EMRIs were captured. The number of events in this longer simulation suggested we have captured approximately 2/3 of the total (for details see the more verbose Wegg 2013).

3.7 General relativistic effects

There are two important GR effects which must be accounted for: GW energy/angular-momentum losses and periapsis precession. Ideally one would either integrate the exact equations of motion in full GR or use the simpler and well-established post-Newtonian approximations. However, it is numerically prohibitive to attempt to use full GR, and the post-Newtonian expansions can be complex, are not separable, and do not have the appropriate divergences at low angular momenta. For example in the 3PN test particle limit the angular momentum at which parabolic orbits 'whirl' (i.e. precession diverges) around a Schwarzschild black hole is $L \approx 4.69\,GM/c$ (compared to the correct value of $L = 4\,GM/c$) and unphysical bound orbits can occur below this (Grossman & Levin 2009).

We instead choose the more straight forward approach of dealing with GW energy/angular-momentum losses and periapsis precession separately in our symplectic integrator.

Recently, Wegg (2012) proposed several pseudo-Newtonian potentials appropriate for the periapsis precession of test particles whose apoapsis lies well beyond the Schwarzschild radius. We use potential B of that work, which balances both accuracy and computational cost.

As mentioned above, we deal with orbital energy and angular momentum losses due to GW emission separately. We deal with both by assuming the stars are on parabolic orbits. These losses are documented and fitting functions for the energy and angular momentum provided by Gair, Kennefick & Larson (2005). We use these fitting functions to determine the change in angular momentum and orbital energy during a complete periapsis passage, and apply these losses discretely at periapsis. The exact implementation is described in Section 4.2.

We note that for stars around Schwarzschild holes our methods remain accurate to arbitrary eccentricity (outside the exponentially narrow 'whirling' region just above $L = 4\,GM/c$ where the precession will be underestimated). The simulations are terminated only if the angular momentum drops below $L \leq L_{\rm plunge} = 4\,GM/c$ as described in Section 4.4.

[1] D. Merritt, personal communication. From fitting to fig. 2 of Merritt et al. (2009).

4 THE SIMULATION

To integrate the orbits of the test particles, we utilize the symplectic integrator described in Preto & Tremaine (1999) and used in Peter (2008, 2009). We use this integrator because

(i) its symplectic nature causes energy to be conserved up to round-off error. This is desirable since spurious energy drifts would, over the many orbits simulated here, directly change the semimajor axis;

(ii) with an appropriate choice of step size (see Section 4.3), orbits in a Keplerian potential are reproduced exactly with only a phase error which is $\mathcal{O}(N^{-2})$.

In particular, we use the version of the integrator used by WB11, extended to take into account both relativistic precession (Section 4.1) and the angular momentum and energy losses due to GW radiation (Section 4.2).

For a detailed discussion of the integrator used in WB11 see that work, and the works on which it was based (Preto & Tremaine 1999; Peter 2008, 2009). Here, we discuss only how the integrator we use differs from that of WB11, along with checks (Section 4.3) and selection criteria (Section 4.4) relevant to this new context.

4.1 Pseudo-Newtonian potential

The prime reason we must use a pseudo-Newtonian potential to model relativistic precession is that the symplectic integrator is constructed by operator splitting and hence requires the Hamiltonian be separable. We therefore cannot evolve particles using post-Newtonian approximations in the equations of motion (as in e.g. Merritt et al. 2011b).

Instead, relativistic precession is included using the pseudo-Newtonian potential labelled as 'potential B' in Wegg (2012). We use this potential since it accurately reproduces the precession of orbits with apoapsis in the far field (i.e. apoapsis $\gg GM/c^2$). Note that the potential of Paczyński & Wiita (1980) does not have this property. In addition, the precession correctly diverges as the orbit approaches $L_{\rm plunge}$ which separates bound orbits from plunges (this occurs at $L = 4GM/c^2$ for parabolic orbits). For reference the complete potential used is

$$U(r) = -\frac{GM}{r_1}\left(\frac{1}{1-\frac{5}{6}\frac{r_{\rm s,1}}{r_1}} + \frac{2}{3}\frac{r_{\rm s,1}}{r_1}\right) - \frac{GM_\bullet}{r_2}\left(\frac{1}{1-\frac{5}{6}\frac{r_{\rm s,2}}{r_2}} + \frac{2}{3}\frac{r_{\rm s,2}}{r_2}\right) - V(r_1)\,, \tag{9}$$

where the numerical subscripts 1 and 2 are used to distinguish quantities measured with respect to the primary and secondary, respectively, r_i is the distance to the ith SMBH, $r_{\rm s,\,i}$ is the Schwarzschild radius of the ith SMBH and $V(r_1)$ is the SP produced by equation (4).

4.2 Gravitational wave losses

When an object passes close to either SMBH, relativistic effects such as energy and angular momentum losses due to gravitational radiation become important. We incorporate these changes into the orbit by stepping out of the symplectic integrator at periapsis and calculating a new velocity vector when the star has passed within $100\,GM/c^2$ of either SMBH. We note the calculations here are for non-spinning Schwarzschild black holes, this assumption is briefly discussed in Section 7.2.

The choice of $100\,GM/c^2$ is motivated by the low losses for stars that remain outside this radius. For our highest mass ratio ($10\,{\rm M}_\odot/10^6\,{\rm M}_\odot = 10^{-5}$), the loss of angular momentum per orbit for a parabolic orbit with periapsis $100\,GM/c$ is $1.9\times10^{-8}GM/c$ and of energy is $1.6\times10^{-11}c^2$. For computational reasons (described below), the highest number of orbits integrated is 5×10^4, and therefore losses for orbits which remain outside of $100\,GM/c^2$ are negligible.

To compute the energy and angular momentum lost during a periapsis passage, we assume the orbits are parabolic. We then relate the angular momentum in the orbit to the energy and angular momentum lost during each periapsis passage using the fitting functions for parabolic orbits from Gair, Kennefick & Larson (2006). In that paper, they compute fitting functions to the energy and angular momentum loss using the Teukolsky equation. For convenience, we provide these fitting functions here:

$$\begin{aligned}\frac{M}{m}\Delta X = \cosh^{-1}&\left[1 + B_0^X\left(\frac{4}{\tilde{r}_{\rm p}}\right)^{N_X-1}\frac{1}{\tilde{r}_{\rm p}-4}\right]\\ &\times\sum_{n=0}^{N}A_n^X\left(\frac{1}{\tilde{r}_{\rm p}}-\frac{4}{\tilde{r}_{\rm p}^2}\right)^n\\ &+\frac{\tilde{r}_{\rm p}-4}{\tilde{r}_{\rm p}^{1+N_X/2}}\sum_{n=0}^{N}C_n^X\left(\frac{\tilde{r}_{\rm p}-4}{\tilde{r}_{\rm p}^2}\right)^n\\ &+\frac{\tilde{r}_{\rm p}-4}{\tilde{r}_{\rm p}^{2+N_X/2}}\sum_{n=0}^{N-1}B_{n+1}^X\left(\frac{\tilde{r}_{\rm p}-4}{\tilde{r}_{\rm p}^2}\right)^n\,,\end{aligned} \tag{10}$$

where X is either the specific energy E/c^2 or the (scaled) specific angular momentum $\tilde{L} = L/(GM/c)$, $\tilde{r}_{\rm p}$ is the periapsis distance in geometrized units, $N_E = 7$, $N_L = 4$, and the A_n^X, B_n^X, and C_n^X are coefficients given in Table 2. In Gair et al. (2006) they note that $N = 2$ is sufficient for better than 0.2 per cent accuracy everywhere. This is the order used in our code. Here, $\tilde{r}_{\rm p}$ is calculated based on the periapsis an orbit would have if it were parabolic and had the measured angular momentum:

$$\tilde{r}_{\rm p} = \frac{\tilde{L}^2}{4}\left(1+\sqrt{1-\frac{16}{\tilde{L}^2}}\right)\,. \tag{11}$$

Note that $\tilde{r}_{\rm p}$ is *not* calculated from the position of the star output by our simulation at its ostensible periapsis, since in the pseudo-Newtonian potential this does not match its relativistic value.

We subtract the energy and angular momentum loss given by equation (10) at the step closest to periapsis. At this step, we calculate a new velocity, $\boldsymbol{v}'$, using the new specific energy, $E' = E + \Delta E$, and specific angular momentum, $L' = L + \Delta L$. Since the position is unchanged, the potential energy is unchanged and

$$v'^2 = v^2 + 2\Delta E\,. \tag{12}$$

Table 2. Coefficients for equation (10).

	$n=0$	$n=1$	$n=2$
A_n^E	−0.318 434	−5.081 98	−185.48
B_n^E	0.458 227	1645.79	8755.59
C_n^E	3.774 65	−1293.27	−2453.55
A_n^L	−2.532 12	−37.6027	−1268.49
B_n^L	0.671 436	1755.51	9349.29
C_n^L	4.624 65	−1351.44	−2899.02

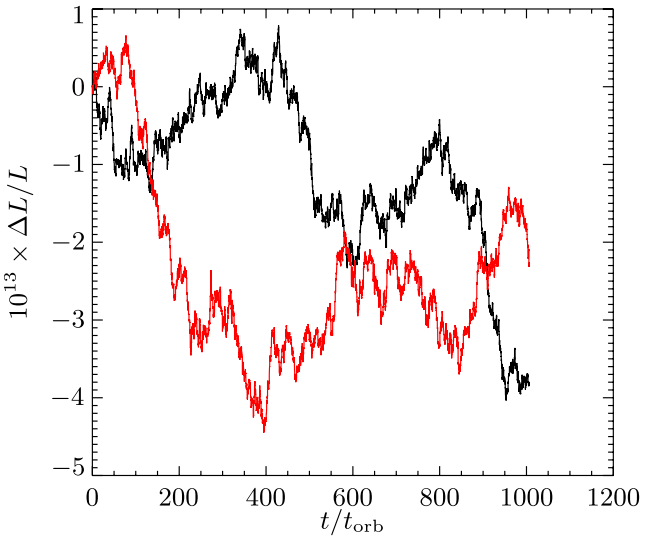

Figure 2. Plot showing the errors in conservation of reduced angular momentum, L, over many orbital periods ($t_{\rm orb}$) of a high-eccentricity ($e = 1 - 10^{-5}$) test particle. The red is without the procedure for calculating the change in $\boldsymbol{v}$ at periapsis, while the black uses equation (15) but with $\Delta L = 0$. The secondary has zero mass for both curves. The errors are still at the level $\Delta L/L \sim 10^{-12}$ indicating that the process of stepping in and out of the symplectic integrator does not inherently introduce significant errors.

The orbital plane remains unchanged for a Schwarzschild black hole and therefore

$$\boldsymbol{L}' = \frac{L + \Delta L}{L}\boldsymbol{L} = \boldsymbol{r} \times \boldsymbol{v}' \,. \tag{13}$$

Taking the dot product of this yields

$$\boldsymbol{r} \,.\, \boldsymbol{v}' = \sqrt{L'^2 - r^2 v'^2}, \tag{14}$$

where we take the positive branch of $\boldsymbol{r} \,.\, \boldsymbol{v}'$ since this corresponds to the outgoing, post-periapsis solution. The cross-product $\boldsymbol{r} \times \boldsymbol{L}'$ yields

$$\boldsymbol{v}' = \frac{1}{r^2}\left[(\boldsymbol{r} \,.\, \boldsymbol{v}')\boldsymbol{r} - \boldsymbol{r} \times \boldsymbol{L}'\right] \,. \tag{15}$$

Equation (15) together with 12, 13 and 14 are then used to calculate the new velocity $\boldsymbol{v}'$ following the periapsis passage.

In Fig. 2, we show the numerical accuracy of this procedure by considering whether L remains constant over many orbits.

4.3 Step size

Preto & Tremaine (1999) show that, for their adaptive symplectic integrator, in a Keplerian potential $U \propto 1/r$ then using a step size $\propto 1/r$ reproduces Keplerian orbits exactly with a phase error whose size is $\mathcal{O}(N^{-2})$, where N is the number of steps per orbit. Since the stars considered here usually evolve in a nearly Keplerian potential we therefore use a step size $\propto U$. The method of choosing the step size has not changed from WB11, except that here we have chosen to have 20 000 steps per orbit.

The phase error introduced by the finite step size in the integrator is along the orbit in a Keplerian potential, i.e. a time error. The dominant error is also along the orbit for the pseudo-Newtonian potential. We expect both errors to be unimportant to both the dynamics and the rates, provided they are small per orbit.

Estimating both phase errors per orbit: (i) the phase error from using a finite step size in the integrator is of the order of $1/N^2 \sim 10^{-8}$. (ii) The phase error in using our pseudo-Newtonian potential compared to the geodesic equation is of the order of $E/c^2 = GM/ac^2$. Our EMRIs are sourced from the dynamics which occur at $a \sim 0.007$ pc. The phase error for these stars is therefore of the order of 7×10^{-6} per orbit.

These errors are also small per orbital period of the secondary SMBH. The pseudo-Newtonian potential accumulates a time error of the order of unity over the entire simulation at $a \sim 0.007$ pc. However, we do not expect this to affect the dynamics.

To check that we are not sensitive to step size we re-ran a simulation with 10 000 steps per orbit. While individual stars evolved differently due to the chaotic nature of some orbits, the number of EMRIs and plunges were statistically unchanged.

4.4 Selection and rejection

Throughout the stars' orbits their periapsis distances and semimajor axes were monitored. The simulation of a given star was stopped if one of three criteria were met: if the star was deemed an EMRI, a plunge, or beyond our computational capacity.

A star was labelled as an EMRI and its evolution terminated if it entered the (*e*)*LISA* band. We choose this to correspond to a semimajor axis where the test particle's orbital period is below 5000 s, i.e. when the semimajor axis is less than

$$a^3 < GM\left(\frac{5000\,\mathrm{s}}{2\pi}\right)^2 \,. \tag{16}$$

The results are not sensitive to this choice of stopping criteria.

A star's simulation was also stopped if the star's angular momentum at periapsis was less than the plunge angular momentum ($L \leq L_{\rm plunge} = 4\,GM/c$). In this case, the star was labelled as a plunge.

In both cases, the star was subsequently reintegrated without a secondary to check that it would not otherwise have become an EMRI or plunge. In particular, stars that over our simulation with no secondary, would have lost more than 5 per cent of their energy to gravitational radiation, or have plunged into the primary hole are discarded and not included in the results.

Finally, due to computational limitations the stars' evolutions were limited to 10^{10} steps. This affects stars with semimajor axes less than 10^{-3} pc (see Figs 7 and 8). These stars are both theoretically (see Section 6.8) and empirically (see Figs 4 and 6) unlikely to form EMRIs.

5 RESULTS AND EMRI RATES

5.1 Introduction to results and rates

We provide a summary of the results of our simulations in Table 3, including both the total number of EMRIs produced and the implied probability of forming an EMRI given the simulation's parameters.

From Table 3, calculating the rates is straightforward. Given a species X of CO (stellar mass black hole, neutron star or white dwarf) the simulation simulates $N_\star$ test particles and outputs the number of EMRIs $N_{\rm EMRI}(X)$ assuming a mass m_X. Then

$$P_{\rm EMRI}(X) \equiv N_{\rm EMRI}(X)/N_\star \tag{17}$$

is the probability that a star of species X eventually becomes an EMRI (Section 5.2).

Table 3. Number of EMRIs and their probabilities in the simulations.

	Parameters				EMRI stars	
Sim #	q^a	$\frac{m_\star}{M_\odot}{}^b$	$N_\star{}^c$	Duration (Myr)^d	$N_{\rm EMRI}{}^e$	$P_{\rm EMRI}{}^f$
1	0.3	10	10^6	1.5	10	1.0×10^{-5}
2	0.3	1	10^6	1.5	1	0.1×10^{-5}
3	0.1	10	10^6	1.4	13	1.3×10^{-5}
4	0.1	1	10^6	1.4	3	0.3×10^{-5}

[a] $q = M_\bullet/M$ is the ratio of the mass of the secondary SMBH to the primary SMBH.
[b] The assumed mass of the stars in $M_\odot$. The mass of the stars is only relevant when the star passes within $100\,GM/c^2$ of one of the SMBHs.
[c] The total number of stars simulated during the run.
[d] The duration of the simulation in megayears.
[e] The total number of EMRIs formed during the simulation.
[f] The probability of a CO of mass $m_\star$ becoming an EMRI.

We then multiply by the expected number of stars in our model cusp of species X assuming some quantity of mass segregation (Section 5.3). This gives the approximate number of events for a given galaxy during the period of time that a secondary SMBH is settling to its stalling radius.

By determining the volumetric rate of galaxies undergoing a gasless merger, $\dot{n}_{\rm merger}(M = 10^6\ M_\odot)$ (Section 5.4), we may produce the predicted EMRI rate density (Section 5.5). That is

$$\mathcal{R}_{\rm EMRI}(X) = P_{\rm EMRI}(X) N_X \dot{n}_{\rm merger}(M = 10^6\,M_\odot)\,. \tag{18}$$

5.2 EMRI merger probability

Each of our simulations has $N_\star = 10^6$, with stars of mass 10 $M_\odot$ or 1 $M_\odot$ (but not both), where we use the former to predict the rates of stellar mass black holes and the latter to predict the rates for both neutron stars and white dwarfs. The probability that an object in a given simulation will turn into an EMRI is calculated using equation (17) and shown in the final column of Table 3.

5.3 Species number density

The number of COs of type X expected as a function of position in the cusp is poorly understood, both observationally and theoretically (Hopman & Alexander 2006; Alexander & Hopman 2009; O'Leary, Kocsis & Loeb 2009). We note that mass segregation would not affect the migration of the binary we calculate in Section 3.6 (although overall density profiles different from $\eta = 1.25$ would). Since the details of mass segregation are uncertain, and most of the EMRIs initiate from a narrow range of semimajor axes, we choose a somewhat novel approach. When estimating the rates we assume the entire cusp at these radii is formed either of stellar mass BHs, or WDs and NSs. The reader can then scale the numbers to their preferred ratios of objects at $a \sim 0.01$ pc. This is possible since in the case considered the rates scale linearly with number of COs. Our fiducial choice here is to scale to the degree of segregation found by Freitag et al. (2006). We tabulate these values in column *b* of Table 4 and use them as our fiducial values.

To determine the number of each stellar remnant in the cusp, we must first consider stellar-mass black holes. In Freitag et al. (2006), they find that there is roughly 10 times as much mass in SBHs than in main-sequence stars (MSSs) close to the SMBH. We assume here that SBH masses are 10 $M_\odot$, which then tells us that there are roughly the same number of SBHs as there are MSSs in the cusp.

Table 4. Approximate mass and number densities of species deep (<0.05 pc) in stellar cusp found by (Freitag et al. 2006).

Species X	$\frac{m_X}{M_\odot}{}^a$	$\frac{\rho_X}{\rho_{\rm MSS}}{}^b$	$\frac{N_X}{N_{\rm MSS}}{}^c$	$N_X{}^d$
Main sequence Star	1	1	1	2×10^5
Stellar-mass black hole	10	∼10	∼1	2×10^5
Neutron star	1	∼0.1	∼0.1	2×10^4
White dwarf	1	∼0.3	∼0.3	6×10^4

[a] Mass of species X in solar masses.
[b] Ratio of density of species X to that of main-sequence stars in the region where EMRIs are formed in our simulations (Freitag et al. 2006).
[c] Ratio of number of stars of species X to the number of main-sequence stars in the region where EMRIs are formed in our simulations.
[d] Total number of species X in the entire stellar cusp if the cusp were to have the same ratio of species X to main-sequences stars as in the region where the EMRIs are sourced in our simulation.

Because most of the mass in the cusp is from the SBHs we can approximate the total number of SBHs by dividing the total mass of the cusp, which we have assumed to be $2 \times 10^6\ M_\odot$, by the mass of the SBHs. This yields 2×10^5 stellar-massed black holes in the cusp. This then tells us there are roughly 2×10^5 MSSs.

As with stellar-massed black holes Freitag et al. (2006) provides the mass density ratios of each stellar type to that of MSSs. Therefore, assuming that NSs and WDs are roughly $1\,M_\odot$, it is trivial to determine the number of each species in the cusp relative to the number of MSSs. Multiplying by $N_{\rm MSS}$ then gives the total number of each species in the cusp:

$$N = \begin{cases} 2 \times 10^5 & \text{for main}-\text{sequence stars} \\ 2 \times 10^5 & \text{for stellar}-\text{mass black holes} \\ 2 \times 10^4 & \text{for neutron stars} \\ 6 \times 10^4 & \text{for white dwarfs} \end{cases}. \tag{19}$$

These calculations are summarized in column *d* of Table 4.

The predicted number of stellar-massed BHs in Table 4 implies an unrealistic total number of stellar-massed BHs in the cusp, but these numbers have been scaled to ensure the correct number of stellar-massed BHs in the inner cusp, from where the EMRIs are sourced. Thus, these numbers produce the correct number of stellar-massed BHs in the relevant region.

5.4 Number density of mergers

We approximate the number density of mergers of SMBHs of mass $10^6\ M_\odot$ and mass ratios between 0.1 and 0.3 by determining the number density of SMBHs of mass $(10^{5.5} - 10^{6.5})\ M_\odot$ and assuming one such SMBH merger per galaxy lifetime.

Aller & Richstone (2002) find a local number density of SMBHs with mass $(10^{5.5}$–$10^{6.5})\ M_\odot$ of $4 \times 10^6\,{\rm Gpc}^{-3}$ (assuming $H_0 = 70\,{\rm km\ s^{-1}Mpc^{-1}}$). Therefore, we approximate

$$\dot{n}_{\rm merger}(M = 10^6\,M_\odot) \sim 3 \times 10^{-4}\,\frac{\rm mergers}{\rm Gpc^3\ yr}\,. \tag{20}$$

We have tacitly assumed above that mergers happen uniformly in time. The assumed constant merger rate (of one merger per galaxy) will probably be fairly accurate for a *LISA* or a *LISA*-like experiment able to detect EMRIs to redshift $z \sim 1$. However, because of the locally falling merger rate they would be over estimates if, for example, EMRIs are detectable only to redshifts of $z \sim 0.1$.

Table 5. Final rates of EMRIs due to SMBH binaries.

q^a	$\mathcal{R}_{\rm EMRI}({\rm yr}^{-1}\,{\rm Gpc}^{-3})^b$		
	SBH	NS	WD
0.3	6×10^{-4}	6×10^{-6}	2×10^{-5}
0.1	8×10^{-4}	2×10^{-5}	5×10^{-5}

[a]The mass ratio of the secondary SMBH to the primary.
[b]Rate of EMRIs due to SMBH binaries for the cases of stellar-mass black holes (SBHs), neutron stars (NSs) and white dwarfs (WDs) assuming that all mergers at rate $\dot{n}_{\rm merger}$ have mass ratio q.

However, there are large uncertainties both in the design of any *LISA* like mission, the detectability of EMRIs, and the cusps and the degree of their relaxation and segregation around $10^6\,{\rm M}_\odot$ SMBHs. The galaxy merger rates used here are chosen due to their simplicity given these uncertainties.

5.5 Final rates

The rate of EMRI production per unit volume, $\mathcal{R}_{\rm EMRI}$, is calculated using equation (18). We use the probability that each star in our simulations becomes an EMRI, $P_{\rm EMRI}$, from Table 3, the numbers of each species, N_X, from Table 4, and the SMBH merger rate, $\dot{n}_{\rm merger}$, from equation (20).

This analysis ultimately yields the following rates

$$\mathcal{R}_{\rm EMRI}(q=0.1)=\begin{cases}8\times10^{-4}\ {\rm yr}^{-1}\,{\rm Gpc}^{-3} & \text{for SBHs}\\ 2\times10^{-5}\ {\rm yr}^{-1}\,{\rm Gpc}^{-3} & \text{for NSs}\\ 5\times10^{-5}\ {\rm yr}^{-1}\,{\rm Gpc}^{-3} & \text{for WDs}\end{cases} \tag{21}$$

and

$$\mathcal{R}_{\rm EMRI}(q=0.3)=\begin{cases}6\times10^{-4}\ {\rm yr}^{-1}\,{\rm Gpc}^{-3} & \text{for SBHs}\\ 6\times10^{-6}\ {\rm yr}^{-1}\,{\rm Gpc}^{-3} & \text{for NSs}\\ 2\times10^{-5}\ {\rm yr}^{-1}\,{\rm Gpc}^{-3} & \text{for WDs}\end{cases}. \tag{22}$$

For reference these rates are given in Table 5.

For context, our overall detection rates are significantly lower than the $\mathcal{R}\sim1\,{\rm yr}^{-1}\,{\rm Gpc}^{-3}$ predicted from isolated SMBHs by Gair et al. (2004). We note that there is presently considerable uncertainly in each rate estimate, and show in Section 7.1 that the rate given here has the prospect of being astrophysically interesting to *LISA*-like missions.

6 STELLAR DYNAMICS: UNDERSTANDING OUR EMRIS AND PLUNGES

The processes which produce the majority of our EMRIs are, dynamically, quite rich. In particular, the interplay between the physical processes of the secular Kozai effect, the SP precession, the competing GR precession and the oscillations of the orbital elements on the secondary SMBH's orbital time-scale is physically intricate and interesting. We elucidate these effects in this section, where we first give a brief description of the Kozai effect (Sections 6.1 and 6.3), then discuss various complicating effects individually (Sections 6.4–6.7), and finally consider the different effects together elucidating their relevance to the EMRI rates (Section 6). Of particular importance are the oscillations in the angular momentum on the time-scale of the secondary (Section 6.6).

6.1 Kozai effect – historical formalism

Instead of giving a detailed description of the Kozai mechanism, something already comprehensively elucidated by the original papers (Lidov 1962; Kozai 1962) and much subsequent work (Holman, Touma & Tremaine 1997; Blaes, Lee & Socrates 2002; Ivanov et al. 2005; Thompson 2011) in various different contexts, we aim to provide in this section the key equations and their consequences relevant to our problem.

In our circumstances, the Kozai mechanism is a secular process whereby the weak quadrupolar tidal force from the secondary SMBH perturbs the orbits of stars around the primary SMBH.

The original theory (Kozai 1962; Lidov 1962) of the Kozai mechanism assumed (in the context of our problem) not only that the semimajor axis of the star is significantly less than that of the secondary SMBH, but also that the star is on what would otherwise be a Keplerian orbit in the absence of the secondary (i.e., general relativistic effects along with effects due to the SP are ignored). Moreover, the Kozai–Lidov theory assumes a purely quadrupolar force and averages over the orbits of both the star and the secondary SMBH. Throughout this subsection, we retain these assumptions.

Here, as with elsewhere in this paper, we will use the following conventions: ω is the argument of periapsis, χ is the longitude of the ascending node, $P_\bullet$ is the period of the secondary, $P_\star$ is the radial period of the star and

$$T_{\rm Kozai}\equiv\frac{2}{3\pi q}\frac{P_\bullet}{P_\star}P_\bullet=\frac{4}{3q}\left(\frac{a_\star}{a_\bullet}\right)^{-3/2}\sqrt{\frac{a_\bullet^3}{GM}} \tag{23}$$

is the widely discussed characteristic time-scale on which the Kozai oscillations occur (e.g. Ivanov et al. 2005).

Starting from the exact equations of motion in the osculating elements, written with the true anomaly as the independent variable, and averaging over both the orbits of the star and the secondary SMBH, Lidov (1962) obtained an insightful set of differential equations (written in the form of Ivanov et al. 2005):

$$T_{\rm Kozai}\frac{{\rm d}a}{{\rm d}t}=0 \tag{24}$$

$$T_{\rm Kozai}\frac{{\rm d}e}{{\rm d}t}=-\frac{5}{2}e\sqrt{1-e^2}\sin^2 i\sin2\omega \tag{25}$$

$$T_{\rm Kozai}\frac{{\rm d}i}{{\rm d}t}=-\frac{5}{4}\frac{e^2\sin(2i)\sin(2\omega)}{\sqrt{1-e^2}} \tag{26}$$

$$T_{\rm Kozai}\frac{{\rm d}\omega}{{\rm d}t}=\frac{2(1-e^2)+5\sin^2(\omega)(\cos^2 i-(1-e^2))}{\sqrt{1-e^2}} \tag{27}$$

$$T_{\rm Kozai}\frac{{\rm d}\chi}{{\rm d}t}=-\frac{\cos i}{\sqrt{1-e^2}}\left\{1+e^2(5\sin^2\omega-1)\right\}. \tag{28}$$

The primary characteristic of the Kozai mechanism is that the star's orbital elements undergo an oscillatory motion which has a period given approximately by $T_{\rm Kozai}$, and which can be of significant magnitude. There are several key outcomes from the above equations:

(i) a, and, therefore, the energy of the star's orbit remains constant (equation 24).

(ii) The eccentricity and inclination reach their extremal values only when $\omega=0,\pm\pi/2$ *or* π (solving equation 25 equal to 0).

In addition to a, equations (24)–(28) admit two further integrals of the motion (Lidov 1962; Kozai 1962):

$$\Theta=(1-e^2)\cos^2 i \qquad \text{is conserved and} \tag{29}$$

$$Q=e^2\left[5\sin^2 i\sin^2\omega-2\right] \qquad \text{is conserved}, \tag{30}$$

which together tell us several things about a star's evolution.

(iii) The z component of the angular momentum is conserved since $L_z = \sqrt{GMa\Theta}$ (equation 29).

(iv) All solutions have $1 - e^2 \geq \Theta$ or, equivalently, $e < \sqrt{1 - \Theta}$ (equation 29).

(v) The eccentricity reaches its maximum (minimum) when the inclination reaches its minimum (maximum) (equation 29).

Many of these points can be seen in the first column of Fig. 3, where we have plotted the evolution of a star whose fate in our $q = 0.3$ and $m_\star = 10\ \mathrm{M}_\odot$ simulation was to become an EMRI (also shown in Figs 1, 4, 6 and 7), except with the SP and GR effects turned off. While the semimajor axis of the star remains constant (first row), L goes through significant oscillations. To avoid confusion, we reiterate that in our simulations we are *not* solving equations (24)–(28), but rather directly integrating the full three-body (non-orbit averaged) calculation (see Section 4 for detailed explanation).

6.2 Conservation of L_z in standard Kozai–Lidov formalism

Point (iii) above has particular importance to our problem. Since L_z is conserved, it must be true that $L \geq L_z$ throughout the evolution of a star. Because EMRIs, tidal disruptions or plunges all require a low total angular momentum of order $L_{\rm plunge}$ or smaller, if a star is to be driven to be an EMRI, tidal disruption or plunge by the Kozai mechanism then we require $L_{\rm plunge} \gtrsim L > L_z$. That is, according to

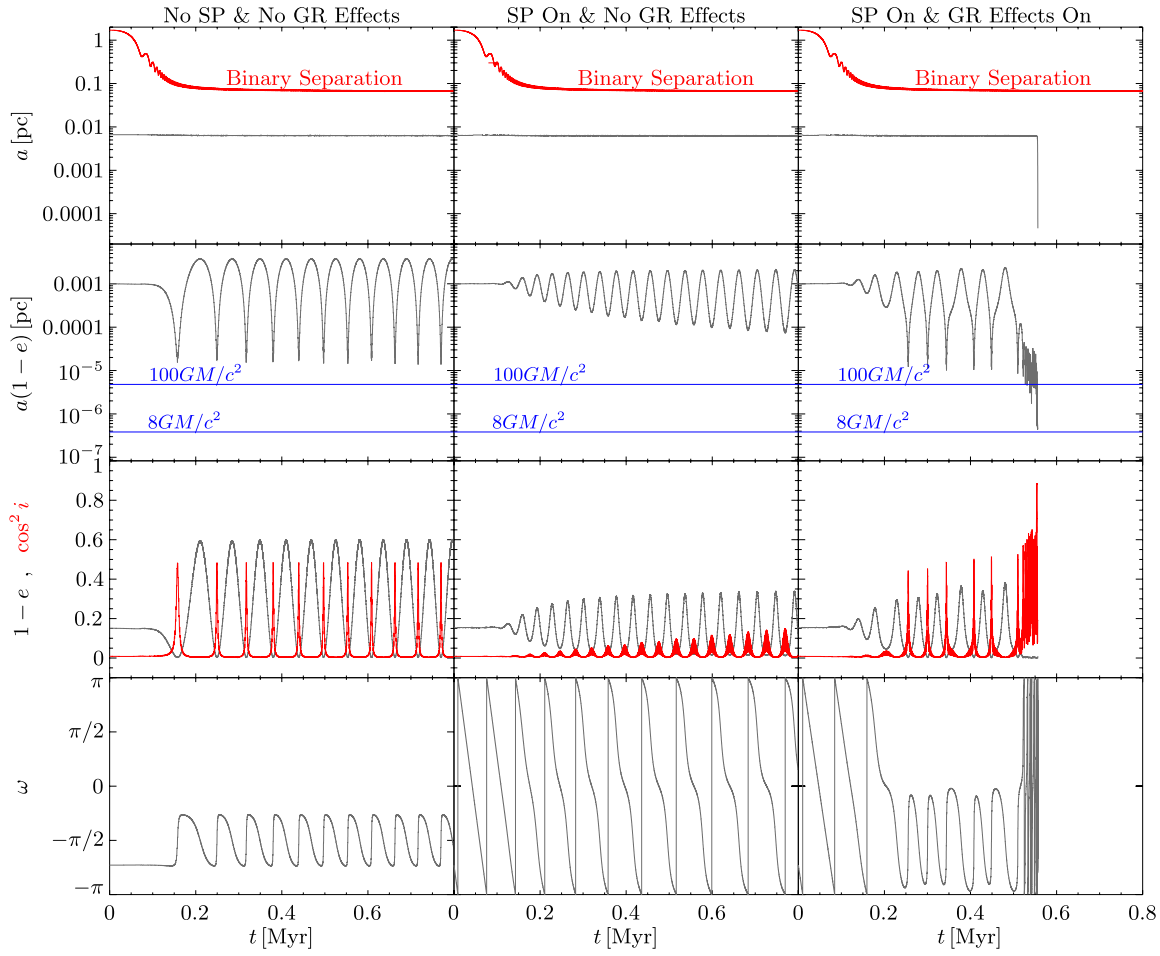

Figure 3. Comparison of Kozai features for a star which turned into an EMRI in one of our simulations evolved with different forms of precession: in the first column, we follow the star without any form of precession (no SP or GR precession); in the second column, we 'turn on' SP precession and in the third column we show the results of the full integration which also has GR precession and GW energy loss. Describing the rows of the plot. In row 1, we plot in charcoal the semimajor axis of a 10 $\mathrm{M}_\odot$ star (the mass is only relevant when GR effects are considered; final column) as a function of time along with the *position* of the secondary plotted in red. In row 2, we plot $a(1 - e)$ in charcoal as a function of time. Also plotted are the lines of constant $a(1 - e) = 8\,GM/c^2$ and $100\,GM/c^2$, the latter being the arbitrary radius where we start calculating the energy loss for the orbit (see Section 4). In row 3, we plot $1 - e$ in charcoal and $\cos^2 i$ in red as a function of time. The product of the two is proportional to L_z^2 which is a conserved quantity in the standard Kozai formalism. In the final row, we plot the argument of periapsis as a function of time. From left to right there are clear changes in the star's orbit as new forms of precession are added. In the first column, once the secondary has reached the stalling radius the star undergoes librating oscillations about $\omega = -\pi/2$ most akin to the traditional Kozai oscillations as described in Section 6.1. In the second column, three clear changes occur: the star begins retrograde precession (row 4) as the SP precession dominates, the oscillation period decreases (rows 2, 3 and 4), and the magnitude of the oscillations is reduced (rows 2 and 3). In the final column (with SP and GR effects on), a very different phenomenon occurs which can be separated into three regions: strong retrograde precession due to the SP, a librating mode in a pseudo-Kozai oscillation where SP and GR precession loosely cancel and a final phase marked by rapid, and apparently chaotic, prograde precession driven by GR. Again, the period of oscillations in e and i are half the precession period. The increasing relevance of GR precession is due not only to having a lower periapsis distance, but also to the effects of the SP being weaker as the eccentricity grows. This star is also marked as a red-outlined gold star in Figs 4, 6 and 7.

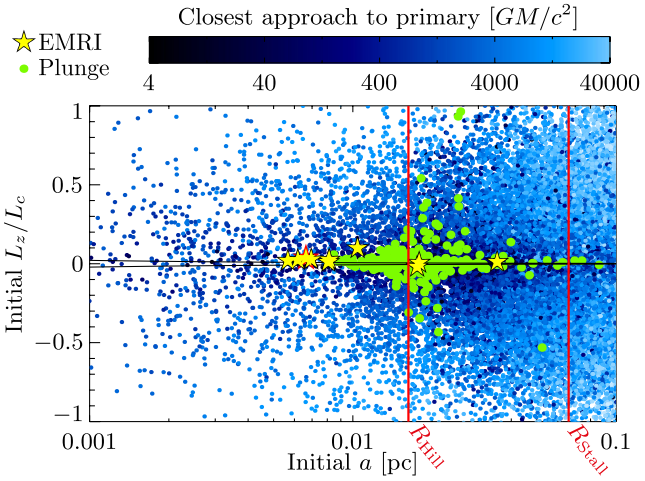

Figure 4. We plot the initial L_z/L_c of our stars as a function of the initial semimajor axis, a. L_c is the circular angular momentum: $L_c^2 = GMa$. In the Kozai formalism (Section 6.1) L_z and a are conserved over a star's evolution. The final stalling radius of the secondary is shown as a vertical red line. The simulation shown has $q = 0.3$ and $m_\star = 10\ \mathrm{M}_\odot$. We encode the shortest distance to the primary SMBH a star reached over its evolution by colour: gold stars represent stars which have turned into EMRIs (Section 4.4), green dots are stars which have plunged into the primary SMBH, and all other stars are coloured in shades of blue with darker blues being shorter distances (see legend, calculated using equation 11). Also plotted in solid black is the Kozai 'wedge'; lines of $L_z = \pm 4\,GM/c$. Inside these lines the standard Kozai formalism (Section 6.1) predicts that it is possible, but not necessary, that a star reaches $L = 4\ GM/c^2$. Thus, it is only inside these wedges that the standard Kozai formalism would predict plunges. Though this condition is not met for the majority of plunges/EMRIs, the clustering around small L_z and at semimajor axes much smaller than the innermost position of the secondary indicate that the Kozai mechanism is important. That many EMRIs and plunges lie outside the Kozai wedge is primarily due to the oscillations on the orbital time-scale of the secondary SMBH (see Section 6.6), and is demonstrated in greater detail in Fig. 6.

the standard Kozai–Lidov formalism, for Kozai to drive a star to plunge, it must be true that

$$L_z \lesssim L_{\rm plunge}\ . \tag{31}$$

Stars with L_z fulfilling this condition are said to lie inside the Kozai wedge (Chen et al. 2009).

The importance of this point is illustrated in Fig. 4 where we plot the outcomes of all stars in the simulation with $q = 0.3$ and $m_\star = 10\,\mathrm{M}_\odot$ as a function of their initial L_z/L_c and a, where L_c is the circular angular momentum. Most plunges and EMRIs originate far from the secondary and come from a relatively narrow region of L_z/L_c, indicating that the Kozai mechanism is important to their evolution.

However, the standard Kozai formalism does not explain the distribution of plunges, and EMRIs, in L_z/L_c. To illustrate this in Fig. 4, we plot the Kozai wedge (lines $L_z = \pm 4\,GM/c$). The reason that most EMRIs and plunges are initially outside (but close to), the Kozai wedge is explained in Section 6.6.

Note that Lithwick & Naoz (2011) and Katz, Dong & Malhotra (2011) have recently shown non-conservation of L_z by the Kozai effect for the restricted three-body case due to the octupole term in the perturbation expansion. In our simulations however, the secondary stalls with a low eccentricity ($e \sim 0.03$), and therefore the octupole term does not secularly perturb the orbit on the time-scales simulated. They may however be important on longer time-scales and with higher eccentricity perturbers.

6.3 Kozai effect – instantaneous Kozai time-scale

In addition to the Kozai time-scale, $T_{\rm Kozai}$, we define a second 'instantaneous Kozai time-scale', $t_{\rm Kozai}$. $T_{\rm Kozai}$ is the characteristic time-scale describing the total period of of a Kozai oscillation. We define $t_{\rm Kozai}$ to be the time that it takes for the orbital angular momentum of the star to change by its own magnitude. Thus, it allows one to understand the relevant time-scale for change *during* an oscillation. This is particularly useful for understanding when GR precession truncates an oscillation at high eccentricity.

The instantaneous Kozai–Lidov time-scale is, to order unity, given by (Chen et al. 2011)

$$\frac{1}{t_{\rm Kozai}} \sim \frac{1}{L}\frac{\mathrm{d}L}{\mathrm{d}t}\,, \tag{32}$$

where the specific angular momentum is given by

$$L = \sqrt{GMa_\star(1-e^2)}\,, \tag{33}$$

and the torque due to the quadrupolar tidal force from the secondary is

$$\left|\frac{\mathrm{d}\boldsymbol{L}}{\mathrm{d}t}\right| = |\boldsymbol{F}\times\boldsymbol{r}| \sim \frac{qGMa_\star^2}{a_\bullet^3}\,. \tag{34}$$

Together equations (32)–(34) give an instantaneous Kozai time-scale of

$$t_{\rm Kozai} \sim \frac{\sqrt{1-e^2}}{2\pi q}\left(\frac{a_\bullet}{a_\star}\right)^3 P_\star \tag{35}$$

$$\sim \frac{\sqrt{1-e^2}}{2\pi q}\frac{P_\bullet^2}{P_\star}. \tag{36}$$

Up to a constant and the factor $\sqrt{1-e^2}$ this is the standard Kozai time-scale given by equation (23). The non-constant factor $\sqrt{1-e^2}$ shows that the time-scale for change in the angular momentum is shorter during periods of high eccentricity. This is because during periods of high eccentricity the orbit has the lowest angular momentum, requiring smaller torques to be significantly altered.

6.4 Apsidal precession

When any form of apsidal precession becomes comparable to $t_{\rm Kozai}$, then the magnitude of the Kozai oscillations is inhibited. This process is sometimes referred to in the literature as the Kozai mechanism being 'de-tuned' (e.g. Thompson 2011). In our context there are two relevant forms of precession which affect the Kozai mechanism: that due to the SP, and that due to GR precession.

The precession due to the non-Keplerian SP results in an apsidal precession per stellar orbit of approximately (e.g. Merritt et al. 2011b)

$$\delta\omega_{\rm SP} \sim -2\pi\frac{\sqrt{1-e^2}}{1+\sqrt{1-e^2}}\frac{M_\star(<a_\star)}{M}\,. \tag{37}$$

Hence, the time-scale to precess though π radians is

$$t_{\phi,\rm SP} \equiv \left|\frac{\pi}{\delta\omega_{\rm SP}}\right| P_\star \sim \frac{1}{2}\frac{1+\sqrt{1-e^2}}{\sqrt{1-e^2}}\frac{M}{M_\star(<a_\star)}P_\star. \tag{38}$$

The mass ratio depends on the cusp model as discussed in Section 3.3.

On the other hand, GR precession has a different dependence. In the far field limit, the per orbit GR precession of a star is given by

$$\delta\omega_{\rm GR} = \frac{6\pi GM}{c^2 a_\star(1-e^2)} = \frac{3\pi}{1-e^2}\frac{r_{\rm S}}{a_\star}. \tag{39}$$

Then, the time-scale to precess through π radians is given by

$$t_{\phi,\rm GR} = \left|\frac{\pi}{\delta\omega_{\rm GR}}\right| P_\star = \frac{1}{3}(1-e^2)\frac{a_\star}{r_{\rm S}}P_\star. \tag{40}$$

It is important to note both that GR precession and SP precession are in opposite directions (equations 37 and 39) and that as the eccentricity of a star's orbit grows, $t_{\phi,\rm SP}$ increases while $t_{\phi,\rm GR}$ decreases (equations 38 and 40).

We can see the individual effects in Fig. 3 where, in the first column we plot the orbital parameters for the example star without either the effects of the SP or GR, in the second column we plot the evolution including only the SP, and in the third column we show the evolution of the full simulation with both the SP and GR effects. One sees that in this case without the GR effects included the SP largely damps the Kozai oscillations, while when they are included the star still reaches the angular momentum expected from the traditional Kozai formalism.

6.5 Extreme apsidal precession

When some non-Keplarian effect, other than Kozai, causes orbital precession on a time-scale $t_{\phi,\rm ext} \equiv \frac{2\pi}{\dot\omega_{\rm ext}}$ which is much shorter than $T_{\rm Kozai}$, then the standard Kozai cycles are truncated on this new shorter time-scale. Because $t_{\phi,\rm ext} \ll T_{\rm Kozai}$, the argument of periapsis ceases to evolve according to equation (27), and instead follows an evolution dictated by this exterior effect [i.e., $\omega(t) \approx \int \dot\omega_{\rm ext}\,{\rm d}t$]. The $\sin 2\omega$ term in the evolution of e and i (equations 25 and 26) mean that both e and i will undergo two oscillations over a time $t_{\phi,\rm ext}$, as expected for the quadrupole perturbation induced by the secondary.

Moreover, given a star with eccentricity e and angular momentum $L(e)$ this reduces the amplitude of the Kozai oscillations to roughly

$$\Delta L \sim L(e)\frac{t_{\phi,\rm ext}}{t_{\rm Kozai}}. \tag{41}$$

That is, stars with low eccentricities will continue to have low eccentricity, but stars with high eccentricity retain their high eccentricity.

In the latter case, if a star reaches a high enough eccentricity that GR precession alone causes the orbit to precess significantly (e.g. by π radians) before the angular momentum can change significantly (e.g. by its own magnitude) then the Kozai oscillations will be stalled at high eccentricity. When this occurs it can be found by taking the ratio of $t_{\phi,\rm GR}$ to $t_{\rm Kozai}$,

$$\frac{t_{\phi,\rm GR}}{t_{\rm Kozai}} \sim 2\sqrt{2}q\left(\frac{a_\star}{a_\bullet}\right)^3\frac{a_\star}{r_{\rm S}}\sqrt{1-e}, \tag{42}$$

and solving for $1-e$

$$1-e = \frac{1}{8}\frac{1}{q^2}\left(\frac{a_\bullet}{a_\star}\right)^6\left(\frac{r_{\rm S}}{a_\star}\right)^2. \tag{43}$$

This has been referred to as the Schwarzschild barrier in the context of resonant relaxation around single SMBHs by Merritt et al. (2011b). In the case of our example star (shown in Figs 1, 3, 4, 6 and 7) this limit to the eccentricity occurs when $1-e \approx 3\times10^{-4}$. In fact, this star does reach this eccentricity, subsequently ceases to oscillate and forming an EMRI on a time-scale too short to be clearly visible in Fig. 3.

Thus, the example star highlights that the case of high eccentricity is of particular importance, since retaining high eccentricity accelerates the rate at which a star inspirals due to GW radiation.

6.6 Fluctuations in L_z on the orbital time-scale of the SMBH binary[2]

In the standard Kozai mechanism, when averaged over the time-scale of the SMBH binary, the component of angular momentum perpendicular to the binary's orbit, L_z, is conserved. However, on shorter time-scales this is not the case. This is because the symmetry about the z-axis is broken on shorter time-scales.

To illustrate this consider a short period over which the secondary SMBH moves negligibly: in this case, the symmetry axis of the quadrupolar tidal force on the star is directed towards the secondary (*not* in the z direction). Therefore, it is this component of the angular momentum (which is perpendicular to z) that is conserved on very short time-scales.

The resultant size of the fluctuations over the binary orbital period will be of the order of[3]

$$\Delta L_{\rm b} \sim \frac{{\rm d}L}{{\rm d}t}\frac{P_\bullet}{4}, \tag{44}$$

where the factor of 4 is to approximately take account of the dominant quadrupolar force, which gives rise to four reverses in sign per orbital period, $P_\bullet$. Using the previously calculated torque (equation 34), we find

$$\Delta L_{\rm b} \sim \frac{qGMa_\star^2}{a_\bullet^3}\frac{P_\bullet}{4} = \frac{\pi}{2}q\left(\frac{a_\star}{a_\bullet}\right)^{3/2}\sqrt{GMa_\star}, \tag{45}$$

$$\equiv \frac{\pi}{2}q\left(\frac{a_\star}{a_\bullet}\right)^{3/2}L_{\rm c}, \tag{46}$$

so that

$$\Delta(1-e) = \frac{\Delta L_{\rm b}}{L_{\rm c}} = \frac{\pi}{2}q\frac{P_\star}{P_\bullet}. \tag{47}$$

Here $L_{\rm c} = \sqrt{GMa_\star}$ is the maximum angular momentum with semi-major axis $a_\star$, the circular angular momentum.

The fluctuations in $\Delta L_{\rm b}$ become vitally important when $\Delta(1-e) \lesssim 1-e$.

$$1-e \lesssim \frac{\pi}{2}q\frac{P_\star}{P_\bullet} = \frac{\pi}{2}q\left(\frac{a_\bullet}{a_\star}\right)^{3/2}. \tag{48}$$

This requirement is analogous to requiring that the variations in the periapsis distance due to the $\Delta L_{\rm b}$ are comparable to the periapsis distance.

If the condition $\Delta(1-e) \lesssim 1-e$ is violated then the secular approximation breaks down. Therefore, whenever the secular Kozai equations are used, it is important to check that, at the highest eccentricities of interest, the size of the oscillations in eccentricity.

We demonstrate this effect in Fig. 5. There we plot $1-e$ for a minimum of $a_\star(1-e)$ in column 1 of Fig. 3 as a function of time. In this case, the star is being evolved without the effects of GR or precession due to the SP so as to best illustrate the effect. In red is the

[2] We note that an earlier version of this manuscript was shared with Antognini et al. (2013) and Katz & Dong (2012) who then nicely showed this effect can be important in hierarchical triples (Antognini et al. 2013), and mergers of white dwarfs in particular (Katz & Dong 2012).

[3] A more precise but complex calculation of $\Delta L_{\rm b}$ can be found in appendix B of Ivanov et al. (2005).

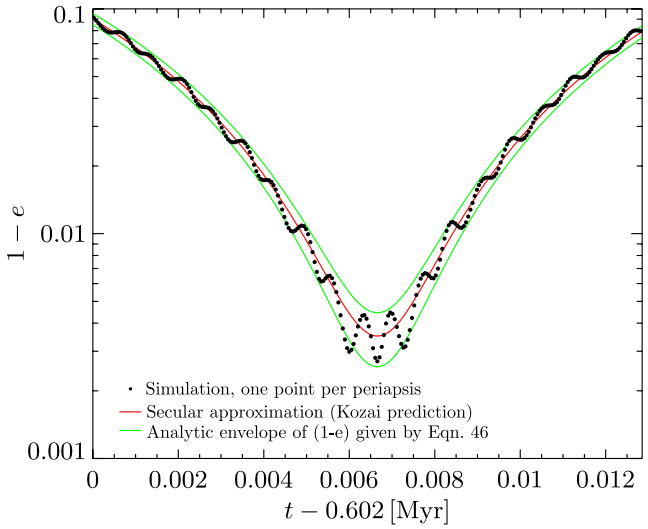

Figure 5. We plot $1 - e$ as a function of time across the peak of the oscillation in eccentricity. In red is the approximate value predicted by the standard Kozai formalism (averaged over the secondary's orbit, equations 24–28), while in green is the expected envelope of oscillations in $1 - e$ over the secondary's orbital time-scale given by equation (48). Each dot represents the value of $1 - e$ calculated by our simulation at apoapsis during the first maximum of the eccentricity in the simulation shown in the first column of Fig. 3 (in which both the SP and the relativistic precession were turned off for clarity). The orbital modulations at the period of the secondary can be significant in these regions.

approximate path predicted by the Kozai formalism, equations (24)–(28), and in green is the predicted envelope given by equation (48). Each dot represents the calculated value of $1 - e$ at periapsis during the integration.

The importance of these oscillations to the evolution of stars in our simulations is best demonstrated in Fig. 6. This is Fig. 4 with a non-normalized azimuthal angular momentum. In this plot, the importance of region where $L_{\rm plunge} + \Delta L_{\rm b}$ is clear and it approximately bounds most EMRIs and plunges. This is because stars with $L_{\rm z} < L_{\rm plunge} + \Delta L_{\rm b}$ region are those that can reach $L_{\rm plunge}$ via the Kozai effect, and therefore plunge into the primary SMBH or become EMRIs.

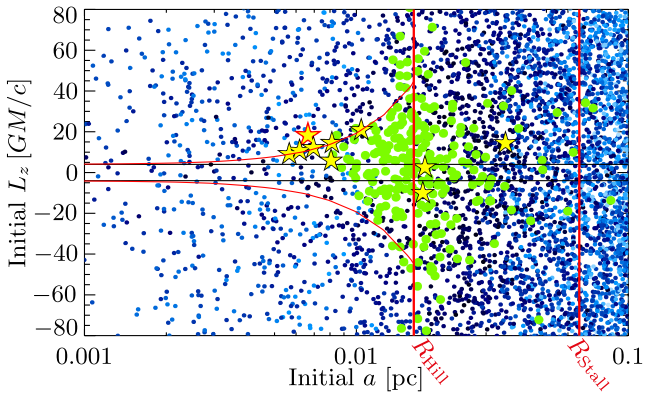

Figure 6. We plot the initial $L_{\rm z}$ as a function of the stars' initial semimajor axes. The symbols and data sets are the same as in Fig. 4. Here, we also show in red $L_{\rm plunge} + \Delta L_{\rm b}$ where $\Delta L_{\rm b}$ are the range of possible oscillations of $L_{\rm z}$ on the SMBH orbital time-scale. As is visible, these oscillations are important for most of the plunges and EMRIs. There is also a visible preference for driving stars with positive $L_{\rm z}$ to become EMRIs or plunges, which is discussed briefly in the text.

Interestingly, there is also a clear asymmetry about $L_{\rm z} = 0$. This is a result of the a symmetry broken by the handedness of the secondary SMBH. When the orbit of the star is in the same sense as that of the secondary SMBH, the star is more likely to reach higher eccentricities and ultimately become a plunge or EMRI. This is likely due to increasing the apparent period of the secondary SMBH during prograde GR precession. This increases the duration over which the torques from the binary are exerted and ultimately the total magnitude of $\Delta L_{\rm b}$.

6.7 Changes in angular momentum on the orbital time-scale of the star

Between periapsis passages a star will undergo a change in angular momentum which is typically of size

$$\Delta L_\star \sim \frac{{\rm d}L}{{\rm d}t} P_\star \sim \frac{qGMa_\star^2}{a_\bullet^3} P_\star = \frac{GMq}{a_\star} \left(\frac{a_\star}{a_\bullet}\right)^3 P_\star , \tag{49}$$

which gives

$$\frac{\Delta L_\star}{L_{\rm c}} = 2\pi q \left(\frac{a_\star}{a_\bullet}\right)^3 = 2\pi q \left(\frac{P_\star}{P_\bullet}\right)^2 . \tag{50}$$

This is naturally of the order of $P_\star/P_\bullet$ smaller than the oscillations on the SMBH binary time-scale given by equation (45). The importance in these oscillations is that while they remain small the star approaches $L_{\rm plunge}$ more smoothly, i.e. the discrete periapsis passages are closely spaced in angular momentum and periapsis distance. This is elucidated in the following subsection.

6.8 Parameter space

To understand the effects of the various mechanisms discussed in this section, we plot the limits that they define in Fig. 7. The initial angular momentum, normalized by $L_{\rm c}$, is plotted against the initial semimajor axis of the stars in our simulation with $q = 0.3$ and $m_\star = 10\,{\rm M}_\odot$. In the upper panel, we plot the initial *total* angular momentum of the stars, while in the lower panel we plot the initial z component of the angular momentum. Stars that result in EMRIs are demarcated by gold stars, stars that plunge by green dots, stars that become unbound by orange dots and all other stars by blue dots.

The secondary stalls at the stalling radius labelled $R_{\rm Stall}$. At this point, the primary has a resultant Hill radius labelled $R_{\rm Hill}$. We define the Hill radius around the primary as the radius inside of which the Jacobi constant cannot be small enough to cross the L_2 Lagrange point beyond the secondary and exit the system (Murray & Dermott 2000). The stars that are unbound and ejected from the system are orange and restricted to semimajor axes greater than the Hill radius.

Lines are shown where the time-scales estimated above are equal: $t_{\rm Kozai} = t_{\phi,\,{\rm SP}}$ (dotted black), $t_{\rm Kozai} = t_{\phi,{\rm GR}}$ (solid black diagonal), $P_\bullet = t_{\phi,{\rm GR}}$ (long dashed black). Also plotted are lines demonstrating the size of changes in angular momentum during the binary's orbit $\Delta L_{\rm b}$ (short dashed black), and over an orbit of the stars $\Delta L_\star$ (dash–dotted black). For orbits close with L close to $L_{\rm plunge}$ then the far field approximation of equation (39) is inaccurate. This is the reason for the curvature of the $t_{\rm Kozai} = t_{\phi,{\rm GR}}$ line, which is calculated using the geodesic equation.

Near or outside the Hill radius stars evolve by strong interactions with the secondary SMBH and the Kozai effect is not relevant. As is visible from the figure, it is less probable that these 'chaotic orbits' turn into plunges or EMRIs than stars farther in which are affected by the Kozai mechanism.

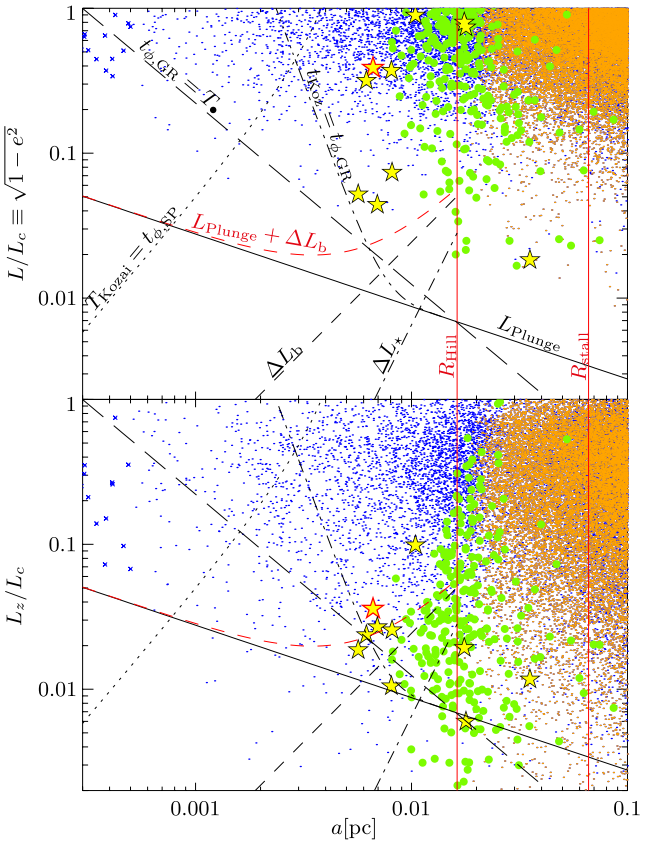

Figure 7. A parameter space plot showing outcomes as function of normalized angular momentum and semimajor axis along with important delimiting lines as discussed in Section 6. Initial L/L_c and L_z/L_c are plotted in the upper and lower panels, respectively. Each star is represented by its outcome: an EMRI (gold star), a plunge (green dot), becoming unbound (orange dot), reaching our computational limit of 10^{10} steps (blue cross), or remaining in the cusp at the conclusion of our simulation (blue dot). The particular simulation shown is $q = 0.3$ and $m_\star = 10\,\mathrm{M}_\odot$.

Well within the Hill radius, the Kozai mechanism is most accurate. By the standard Kozai formalism no star with an initial L_z much greater than L_{plunge} should plunge (or form an EMRI), since L_z is conserved. However, due to oscillations in L, (ΔL_{b}) which occur on the binary orbital time-scale and are not accounted for in the Kozai formalism stars with higher L_z can still become plunges or EMRIs if $L_z \lesssim L_{\mathrm{plunge}} + \Delta L_{\mathrm{b}}$.

The plunges and EMRIs lie to the right of the Schwarzschild barrier ($t_{\mathrm{Kozai}} = t_{\phi,\mathrm{GR}}$) since to the left of this line GR precession dominates the evolution and it is not possible to reach low angular momenta before the orbit precesses and the tidal torque is reversed.

Moreover, in the region with a small but to the right of $t_{\mathrm{Kozai}} = t_{\phi,\mathrm{GR}}$, the changes of angular momentum over each orbit ($\Delta L_\star$) are small and therefore stars gradually approach L_{plunge}. As a result these stars undergo close periapsis passages and lose their energy to gravitational radiation instead of directly plunging. To the right of this region, with larger a, the change in angular momentum on each orbit becomes larger, and stars are more likely to plunge directly into the primary than become EMRIs.

6.9 Synopsis

There are essentially three different ways of producing EMRIs in the context of widely separated binary SMBHs: (1) single or multiple strong interactions with the secondary SMBH which cause the CO to fortuitously pass close to the primary; (2) Kozai oscillations mixed with oscillations on the time-scale of the secondary which drive the star to high eccentricity and has some significant probability of plunging but instead has a close passage and (3) stars which are also driven to high eccentricity from Kozai oscillations mixed with oscillations on the time-scale of the secondary, but approach the Schwarzschild barrier before, but in the near vicinity of L_{plunge}. In our simulations, the first of these methods is sub-dominant, and so we focus on the latter two.

In both cases, the initial process is the same and so we shall describe them together. The star must begin with a low L_z such that $L_z \leq L_{\mathrm{plunge}} + \Delta L_{\mathrm{b}}$. This alone is necessary but not sufficient to ensure that a star will reach L_{plunge}. Secondly, the star should have a semimajor axis which is at most a factor of a few smaller than R_{Stall}. This avoids the strong scatterings by the secondary that are most likely to eject the star from the system, and instead results in Kozai–Lidov oscillations. However, the semimajor axis of the star cannot be so low that the Kozai period becomes too long and GR precession dominates the evolution ($t_{\mathrm{Kozai}} > t_{\phi,\mathrm{GR}}$) before reaching low angular momenta. In this case, the orbit will precess and the tidal torque that drives the Kozai–Lidov oscillations will be reversed well before L_{plunge}. GW radiation therefore cannot act efficiently to drive the star to be an EMRI.

In our simulations, we find a 'sweet spot' where the semimajor axis is just larger than the Schwarzschild barrier. In this region, the changes in angular momentum between periapsis passages are small ($\Delta L_\star \ll L_{\mathrm{plunge}}$). The star therefore has close periapsis passages in which it can radiate orbital energy in GWs, forming an EMRI before plunging beyond the Schwarzschild radius. At larger semimajor axes the change in periapsis distance per orbit is larger, and stars are more likely to plunge directly into the primary SMBH.

7 DISCUSSION

7.1 EMRI rates

Under the previous design of *LISA* EMRIs consisting of a $10^6\,\mathrm{M}_\odot + 10\,\mathrm{M}_\odot$ black hole system would be detectable to a redshift of $z \sim 1$ (dimensionless spin $a/M = 0.9$, averaged over orientations, Amaro-Seoane et al. 2007) giving a comoving detection volume of $160\,\mathrm{Gpc}^3$. The rate of EMRIs from SMBH binaries estimated here of $\mathcal{R}_{\mathrm{EMRI}} = 8 \times 10^{-4}\mathrm{yr}^{-1}\,\mathrm{Gpc}^{-3}$ (Table 5), gives a detection rate of $\sim 0.12\,\mathrm{yr}^{-1}$, and therefore ~ 0.6 over a five year mission.

This is particularly interesting since EMRI waveforms contain information about the presence of both gas (Narayan 2000; Yunes et al. 2011b) and the secondary SMBH (Yunes et al. 2011a). The importance of gas is significant, since due to the same mechanisms discussed here, a large number of tidal disruptions are also expected (Chen, Liu & Magorrian 2008; Wegg & Bode 2011; Chen et al. 2011). Thus, any EMRI observed with the signal of a secondary SMBH in its waveform formed by the mechanisms discussed here are likely to be in the presence of gas.

It is important to note that our rates are proportional to the number density of COs at about $R_{\mathrm{Stall}}/10 \sim 0.01\,\mathrm{pc}$. Note that this is in contrast to the standard picture of isolated SMBH EMRI formation where the rate scales with the product of the number density of COs and that of stars (e.g. Hopman 2009). Therefore, in the fully mass segregated case, the isolated SMBH EMRI formation rate scales with the square of the number density of COs. We discuss

some of our assumptions which affect the number density of COs in Section 7.2.

There is another key consequence of the EMRI formation mechanism presented here, which is outside the scope of this work. In the standard picture of EMRI formation stars must scatter to a state with low overall L, while in the Kozai picture stars need only a low L_z (i.e. the standard loss cone is instead the entire Kozai wedge, see Figs 4 and 6). Thus, for the duration of the secondary's time at the stalling radius, interactions (such as star–star scattering, or non-conservation of L_z due to the octopole term Lithwick & Naoz 2011) need only drive stars to low L_z (or more accurately low $L_z + \Delta L_b$, see Section 6.8) for them to be able to form EMRIs under the Kozai mechanism. This situation is similar to the predicted increased rates of tidal disruption in axisymmetric nuclei. In this case, the rates are increased by a factor of a few from spherical nuclei (Magorrian & Tremaine 1999; Vasiliev & Merritt 2013). We therefore conservatively expect an increase of at least this factor in the EMRI rate while the secondary SMBH is stalled. However, there is at least one reason to suspect rate increase would be higher than this. The oscillations on the time-scale of the SMBH binary (Section 6.6) do not occur in axisymmetric nuclei, and these expand the size of the loss cone. The situation warrants further investigation but is beyond the scope of this work.

7.2 Assumptions

Schwarzschild Black Holes. Throughout this work, in common with the vast majority of studies on the formation of EMRIs, we neglect the spin of the SMBH. This is a short coming that is only beginning to be overcome (Amaro-Seoane, Sopuerta & Freitag 2013). We make this choice for simplicity, since there is increasing observational evidence that at least some SMBHs have significant spin (Brenneman & Reynolds 2006). Apart from very close passages, even in the presence of spin, the precession will be dominated by the Schwarzschild terms (Merritt et al. 2009). Instead the largest effect on this work would be Lense–Thirring precession of the star's orbital plane since, if the BH spin is not aligned with the orbital plane, this would result in non-conservation of L_z. We speculate this could therefore increase the rate of EMRIs and plunges since more stars can potentially undergo Kozai oscillations which result in close BH encounters. To lowest order in v/c the angular momentum of a test particle in the Kerr metric precesses due to Lense–Thirring precession at a rate (Merritt 2013, we neglect the quadrupolar term in this order of magnitude estimate)

$$\frac{\mathrm{d}\boldsymbol{L}}{\mathrm{d}t} = \frac{4\pi}{P_\star}\left(\frac{GM}{Lc}\right)^3 (\boldsymbol{\chi}\times\boldsymbol{L}), \tag{51}$$

where $\boldsymbol{\chi}$ is the dimensionless spin vector of the black hole. Over n orbits, we therefore expect a change in L_z of

$$\Delta L_z \approx 4\pi n\left(\frac{GM}{Lc}\right)^3 (\boldsymbol{\chi}\times\boldsymbol{L})_z. \tag{52}$$

The majority of the EMRIs have initial semimajor axis $a \approx 0.007$ pc and have $n \approx 20\,000$ orbits over the entire length of our simulations. For a favourably oriented spinning hole then, over our simulation, stars at this semimajor axis change their L_z by

$$\frac{\Delta L_z}{GM/c} \approx \frac{1.7\chi}{1-e^2}. \tag{53}$$

Therefore, even over the $\approx$1 Myr length of our simulations a significant fraction of stars at this radius could have their L_z secularly changed by of the order of the size of the loss cone by a spinning black hole. These perturbations would continue for the entire length of time that the binary is stalled.

Cusp Profile. One of the major factors in determining the rates is the stellar distribution. In our simulations, we use an η-model (Tremaine et al. 1994) of a spherical stellar cusp with a central SMBH to establish the stellar distribution (see Section 3.3). This is a self-consistent family of models of a stable isotropic stellar cusp. In our simulations, we have chosen $\eta = 1.75$, the value appropriate for a relaxed stellar cusp. However, there is a complication: the galaxy where we can best resolve the inner parsec is our own Milky Way, and as yet there is no consensus on the existence of a cusp (Buchholz, Schödel & Eckart 2009; Do et al. 2009; Bartko et al. 2010; Yusef-Zadeh, Bushouse & Wardle 2012). An alternative interpretation to a lack of a steep visible cusp is that a density cusp is present in the Galactic Centre, but is 'dark' as a result of mass segregation causing the density to be dominated by COs (Freitag et al. 2006; Preto & Amaro-Seoane 2010). Our rates scale roughly linearly with the number density of stellar mass black holes at $R_{\rm stall}/10 \sim 0.01$ pc, allowing them to easily be rescaled to other cusp profiles (and other CO number densities).

Stellar Interactions. We have not considered relaxation processes such as those due to star–star scattering or star-bulk scattering.

The time-scale for relaxation via star–star scattering is approximately 1 Gyr at r_c (Amaro-Seoane & Preto 2011), much longer than the duration of our simulations, and is not a strong function of r in the cusp (Alexander 2005). However, care must be taken. This approximation is not as accurate as might be assumed because the time-scale to change angular momentum by of the order of itself will be reduced for high-eccentricity orbits by a factor of $\sim(1-e^2)$ (Hopman & Alexander 2005). Therefore, for the highest eccentricity stars in our simulation relaxation could be beginning to become non-negligible.

In the case of star-bulk relaxation such as that due to resonant relaxation or asymmetric bulges the time-scales can be much shorter. For instance, consider resonant relaxation. In this case, the comparable time-scale to $t_{\rm Kozai}$ is given by (Merritt et al. 2011a)

$$t_{\rm rr} = \sqrt{N_\star(<a_\star)}\frac{M}{M_\star(<a_\star)}\frac{P_\star}{2\pi}\sqrt{1-e^2}\,. \tag{54}$$

Here, $N_\star(<a_\star)$ is the number of stars inside the semimajor axis of the test star. Equating $t_{\rm rr}$ to $t_{\rm Kozai}$, we can solve for the semimajor axis where the two effects are comparable:

$$a_{\rm rr} = 0.004\left(\frac{R_{\rm Stall}}{0.07\,\mathrm{pc}}\right)^{24/19}\left(\frac{q}{0.3}\right)^{-8/19}\left(\frac{M/m_\star}{10^5}\right)^{-4/19}\mathrm{pc}. \tag{55}$$

Inside of $a_{\rm rr}$ resonant relaxation would be the dominant form of precession while further out the Kozai torques would dominate the evolution. While $a_{\rm rr}$ is about a factor of 2 smaller than where our innermost EMRIs are sourced it could have an impact on our results. However, this is beyond the scope of this work.

SMBH merger rate. While in recent years there has been significant progress in understanding the merger rates of SMBHs, there still remains a great deal of uncertainty. Indeed, this is one of the unknowns that *LISA* or a *LISA*-like experiment would estimate. Here, we have made the crude approximation that every $10^6\,\mathrm{M}_\odot$ SMBH will undergo one major merger per Hubble time with a constant probability over time. While it is certain that neither of these assumptions is quite right, we expect the uncertainties here to be minimal when compared to those relating to the stellar cusp, or, potentially, the lack thereof. For this reason, we have chosen simplicity over false precision.

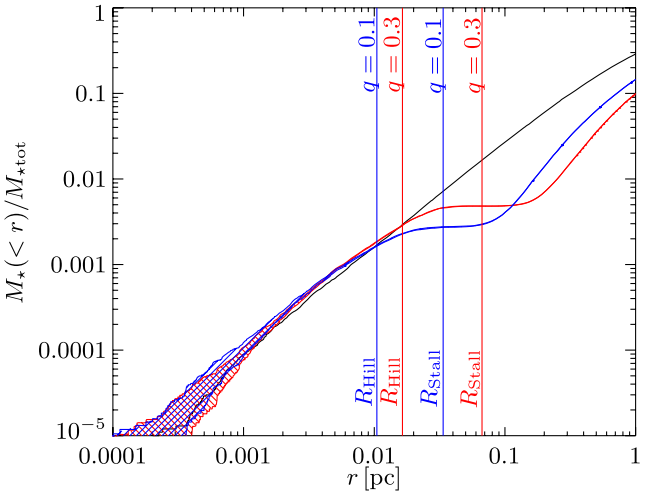

Figure 8. We plot the stellar mass interior to a given radius normalized to the total stellar mass, $M_\star(<r)/M_{\star\rm tot}$. In black, we plot the initial cumulative stellar mass (cf. equation 5), while in blue we plot the cumulative stellar mass at the end of the simulation for the $q = 0.1$, $m_\star = 10$ M$_\odot$ run, and in red we plot the cumulative stellar mass at the end of the simulation for the $q = 0.3$, $m_\star = 10$ M$_\odot$ run. Note that the initial conditions for all runs are the same. The only difference between the outcomes of the runs with the same q but different stellar masses is due to those stars which go within $100\,GM/c^2$, only a small fraction of all stars. Thus, the cumulative stellar mass for the runs with $m_\star = 1$ M$_\odot$ are virtually the same as the 10 M$_\odot$ counterparts with the same q. The hatched regions are stars that had not completed the full simulation within the preset limit of 10^{10} steps. For reference, we also plot the stalling radii of the secondary as vertical lines.

Invariant stellar potential. One inconsistency of our methodology is the assumption that the SP does not evolve with time, though the stars' orbits do. To demonstrate the possible effect of such an assumption, we plot the mass interior to a given radius as a function of radius in Fig. 8. There the solid black line is the initial distribution given by equation (5), the red solid line is the curve for the $q = 0.3$ and $m_\star = 10$ M$_\odot$ simulation, and the blue solid curve is for the $q = 0.1$ and $m_\star = 10$ M$_\odot$ simulation. The mass of the star has little effect on these curves. The filled region represents stars that required more than 10^{10} steps to complete the simulation and were therefore terminated. From Figs 4 and 6, most EMRIs originate from $\approx 10^{-2}$ pc and at this position the mass interior has not changed significantly. Thus, this assumption would not likely have a significant impact on our findings.

8 CONCLUSION

We have considered the possibility of EMRIs that form as a result of a secondary SMBH inspiraling towards a primary SMBH. Using a symplectic integrator to follow the paths of 10^6 non-interacting stars around a primary 10^6 M$_\odot$ SMBH with various values for both the stellar mass and an inspiraling secondary SMBH, we have reached several conclusions.

(i) EMRIs can be formed by binary SMBH systems with numbers which could detectable by future space-based GW missions.

(ii) Frequently overlooked, oscillations on the time-scale of the secondary SMBH, and which deviate from the traditional Kozai–Lidov mechanism, are fundamental to the formation of almost all EMRIs and plunges.

(iii) The region of parameter space where precession due to GR, $t_{\phi,\rm GR}$, and the precession due to the Kozai–Lidov mechanism, $t_{\rm Kozai}$, are comparable (the Schwarzschild barrier: $t_{\phi,\rm GR} = t_{\rm Kozai}$) causes important dynamical effects.

(iv) When a star has a semimajor axis such that $t_{\rm Kozai} < t_{\phi,\rm GR}$, neither EMRIs nor plunges are possible since the precession rate due to GR will increase before the angular momentum of the star falls sufficiently to plunge or become an EMRI.

(v) When a star has a semimajor axis such that $t_{\rm Kozai} > t_{\phi,\rm GR}$, EMRIs are formed most often when the star has a smaller semimajor axis, since it will gradually approach the plunge angular momentum (small $\Delta L_\star$). At higher semimajor axes plunges are more likely.

It is also interesting that the formation of EMRIs by the channel described here is verifiable. While we have shown that it is possible for EMRIs to be formed in SMBH binaries, it has also been shown that, if such an EMRI were to form and be detected, it is possible that the waveform provides information about the mass of the secondary SMBH and the binary separation (Yunes et al. 2011a). This is of particular interest since, by inferring the existence of an SMBH binary at wide separation, it would extend the range of SMBH binary separations to which low frequency GW detectors are sensitive.

ACKNOWLEDGEMENTS

We gratefully acknowledge a significant amount of guidance from Sterl Phinney, many insights regarding resonant relaxation from David Merritt and useful conversations with Sotiris Chatzopoulos, Chris Hirata, Smadar Naoz and Michele Vallisneri.

Support for this work was provided by NASA BEFS grant NNX-07AH06G.

REFERENCES

Alexander T., 2005, Phys. Rep., 419, 65
Alexander T., Hopman C., 2009, ApJ, 697, 1861
Aller M. C., Richstone D., 2002, AJ, 124, 3035
Amaro-Seoane P., Preto M., 2011, Classical Quantum Gravity, 28, 094017
Amaro-Seoane P., Gair J. R., Freitag M., Miller M. C., Mandel I., Cutler C. J., Babak S., 2007, Classical Quantum Gravity, 24, 113
Amaro-Seoane P. et al., 2012, GW Notes, 6, 4
Amaro-Seoane P., Sopuerta C. F., Freitag M. D., 2013, MNRAS, 429, 3155
Antognini J. M., Shappee B. J., Thompson T. A., Amaro-Seoane P., 2013, preprint (arXiv:1308.5682)
Bahcall J. N., Wolf R. A., 1976, ApJ, 209, 214
Barack L., Cutler C., 2004, Phys. Rev. D, 69, 82005
Bartko H. et al., 2010, ApJ, 708, 834
Begelman M. C., Blandford R. D., Rees M. J., 1980, Nature, 287, 307
Binney J., Tremaine S., 2008, in Binney J., Tremaine S., eds, Galactic Dynamics, 2nd edn. Princeton Univ. Press, Princeton, NJ
Blaes O., Lee M. H., Socrates A., 2002, ApJ, 578, 775
Brenneman L. W., Reynolds C. S., 2006, ApJ, 652, 1028
Buchholz R. M., Schödel R., Eckart A., 2009, A&A, 499, 483
Chen X., Liu F. K., Magorrian J., 2008, ApJ, 676, 54
Chen X., Madau P., Sesana A., Liu F. K., 2009, ApJ, 697, L149
Chen X., Sesana A., Madau P., Liu F. K., 2011, ApJ, 729, 13
Côté P. et al., 2004, ApJS, 153, 223
Do T., Ghez A. M., Morris M. R., Lu J. R., Matthews K., Yelda S., Larkin J., 2009, ApJ, 703, 1323
Freitag M., Amaro-Seoane P., Kalogera V., 2006, ApJ, 649, 91
Gair J. R., Barack L., Creighton T., Cutler C., Larson S. L., Phinney E. S., Vallisneri M., 2004, Classical Quantum Gravity, 21, 1595
Gair J. R., Kennefick D. J., Larson S. L., 2005, Phys. Rev. D, 72, 84009
Gair J. R., Kennefick D. J., Larson S. L., 2006, ApJ, 639, 999
Ghez A. M. et al., 2008, ApJ, 689, 1044
Grossman R., Levin J., 2009, Phys. Rev. D, 79, 043017
Hils D., Bender P. L., 1995, ApJ, 445, L7

Holman M., Touma J., Tremaine S., 1997, Nature, 386, 254
Hopman C., 2009, Classical Quantum Gravity, 26, 094028
Hopman C., Alexander T., 2005, ApJ, 629, 362
Hopman C., Alexander T., 2006, ApJ, 645, L133
Hughes S. A., 2009, ARA&A, 47, 107
Ivanov P. B., Polnarev A. G., Saha P., 2005, MNRAS, 358, 1361
Katz B., Dong S., 2012, preprint (arXiv:1211.4584)
Katz B., Dong S., Malhotra R., 2011, Phys. Rev. Lett., 107, 181101
Kozai Y., 1962, AJ, 67, 591
Levin Y., 2003, preprint (astro-ph/0307084)
Levin Y., Beloborodov A. M., 2003, ApJ, 590, L33
Lidov M. L., 1962, Planet. Space Sci., 9, 719
Lithwick Y., Naoz S., 2011, ApJ, 742, 94
Magorrian J., Tremaine S., 1999, MNRAS, 309, 447
Menou K., Haiman Z., Kocsis B., 2008, New Astron. Rev., 51, 884
Merritt D., 2013, Dynamics and Evolution of Galactic Nuclei. Princeton Univ. Press, Princeton, NJ
Merritt D., Schnittman J. D., Komossa S., 2009, ApJ, 699, 1690
Merritt D., Alexander T., Mikkola S., Will C., 2011a, Phys. Rev. D, 81, 62002
Merritt D., Alexander T., Mikkola S., Will C., 2011b, Phys. Rev. D, 84, 44024
Miller M. C., Freitag M., Hamilton D. P., Lauburg V. M., 2005, ApJ, 631, L117
Milosavljević M., Merritt D., 2003, ApJ, 596, 860
Murray C. D., Dermott S. F., 2000, Solar System Dynamics. Cambridge Univ. Press, Cambridge
Narayan R., 2000, ApJ, 536, 663
O'Leary R. M., Kocsis B., Loeb A., 2009, MNRAS, 395, 2127
Paczyński B., Wiita P., 1980, A&A, 88, 23
Peter A. H. G., 2008, PhD thesis, Princeton University
Peter A. H. G., 2009, Phys. Rev. D, 79, 103531
Peters P. C., 1964, Phys. Rev. D, 136, 1224
Preto M., Amaro-Seoane P., 2010, ApJ, 708, L42
Preto M., Tremaine S., 1999, AJ, 118, 2532
Ryan F. D., 1997, Phys. Rev. D, 56, 1845
Sesana A., Vecchio A., Eracleous M., Sigurdsson S., 2008a, MNRAS, 391, 718
Sesana A., Haardt F., Madau P., 2008b, ApJ, 686, 432
Thompson T. A., 2011, ApJ, 741, 82
Tremaine S., Richstone D. O., Byun Y.-I., Dressler A., Faber S. M., Grillmair C., Kormendy J., Lauer T. R., 1994, AJ, 107, 634
Vasiliev E., Merritt D., 2013, ApJ, 774, 87
Wegg C., 2012, ApJ, 749, 183
Wegg C., 2013, PhD thesis, California Institute of Technology
Wegg C., Bode J. N., 2011, ApJ, 738, L8
Yunes N., Miller M. C., Thornburg J., 2011a, Phys. Rev. D, 83, 44030
Yunes N., Kocsis B., Loeb A., Haiman Z., 2011b, Phys. Rev. Lett., 107, 171103
Yusef-Zadeh F., Bushouse H., Wardle M., 2012, ApJ, 744, 24

This paper has been typeset from a TEX/LATEX file prepared by the author.